Titre: Title:	Numerical simulation of merging of two rising bubbles with different densities and diameters using an enhanced Volume-Of-Fluid (VOF) model
Auteurs: Authors:	Faroogh Garoosi, Tarek Merabtene, & Tew-Fik Mahdi
Date:	2022
Type:	Article de revue / Article
Référence: Citation:	Garoosi, F., Merabtene, T., & Mahdi, T.-F. (2022). Numerical simulation of merging of two rising bubbles with different densities and diameters using an enhanced Volume-Of-Fluid (VOF) model. Ocean Engineering, 247, 110711 (27 pages). https://doi.org/10.1016/j.oceaneng.2022.110711

URL de PolyPublie: PolyPublie URL:	https://publications.polymtl.ca/10169/
Version:	Version finale avant publication / Accepted version Révisé par les pairs / Refereed
Conditions d'utilisation: Terms of Use:	Creative Commons Attribution-Utilisation non commerciale-Pas d'oeuvre dérivée 4.0 International / Creative Commons Attribution-NonCommercial-NoDerivatives 4.0 International (CC BY-NC-ND)

Titre de la revue: Journal Title:	Ocean Engineering (vol. 247)
Maison d'édition: Publisher:	Elsevier
URL officiel: Official URL:	https://doi.org/10.1016/j.oceaneng.2022.110711
Mention légale: Legal notice:	© 2022. This is the author's version of an article that appeared in Ocean Engineering (vol. 247) . The final published version is available at https://doi.org/10.1016/j.oceaneng.2022.110711. This manuscript version is made available under the CC-BY-NC-ND 4.0 license https://creativecommons.org/licenses/by-nc-nd/4.0/

Numerical simulation of merging of two rising bubbles with different densities and diameters using an enhanced Volume-Of-Fluid (VOF) model

Faroogh Garoosi[*,a], Tarek Merabtene[b], Tew-Fik Mahdi[a]

[a]Department of Civil, Geological and Mining Engineering, Polytechnique Montreal, Montreal, Quebec, Canada

[b]Department of Civil and Environmental Engineering, University of Sharjah. P. O.Box 27272 Sharjah. United Arab Emirates

Corresponding author: faroogh.garoosi@polymtl.ca,

Second author: tmerabtene@sharjah.ac.ae

Third author: tewfik.mahdi@polymtl.ca

Abstract

In this study, the transient evolution of two rising bubbles with different densities is investigated numerically using an enhanced version of the VOF model, aiming to establish an state-of-the-art benchmark solutions and up-to-date data set for CFD validations. The simulations are performed on the staggered grid system where a novel third- order accurate monotone convection scheme is applied for the discretization of the convection terms in Navier-Stokes and volume fraction equations while the semi-iterative PISOC algorithm (a combined version of the classical PISO and Chorin's model) are used to solve the pressure-velocity coupling. To reduce the false diffusion errors and mitigate smearing of interface thickness in the regions of physical discontinuities, the interface compression technique is also incorporated into the transport equation. To further enhance the accuracy of the numerical solutions, the idea of Piecewise Linear Interface Calculation (PLIC) based on the ELVIRA technique (Efficient Least-square Volume-of-fluid Interface Reconstruction Algorithm) is also utilized for the interface reconstruction and accurate implementation of surface tension force. The validity and accuracy of the enhanced VOF model is further demonstrated against a series of challenging benchmark cases including draining of liquids from the storage tank (tank draining), single rising bubble, three-phase Rayleigh-Taylor Instability and dam-break flows over dry and wet beds. The comparison of the obtained results with previously published data vividly demonstrates the superiority of the proposed method over the standard VOF/Level-Set models in handling multiphase/multi-fluid flow problems with large topological changes. In the last stage, the morphology and hydrodynamic characteristics of merging of two rising bubbles with different densities and diameters are examined and analyzed in details. The results show that, the initial/final deformations and the subsequent steady-state rise of two bubbles are remarkably influenced by the diameters of leading (upper) and trailing (lower) bubbles.

Keywords: Monotone convection scheme; PISOC algorithm; Multiphase flows; VOF model; merging of two rising bubbles;

Nomenclature

C_{φ}	Interface compression coefficient
F_g	gravity force
F_{ST}	surface tension force
g	Gravitational acceleration, ms^{-2}
H	enclosure height, m
L	Length of the enclosure (m)
$\mathbf{n}$	interface normal vector
p	pressure, Nm^{-2}
P	dimensionless pressure
t	time (s)
t^*	dimensionless time, ($t\alpha/H^2$)
u,v	velocity components, ms^{-1}
$\boldsymbol{u}_R$	artificial compressive velocity, ms^{-1}

Re	Reynolds number
U, V	Dimensionless velocity components
x,y	Cartesian coordinates, *m*
X, Y	Dimensionless Cartesian coordinates
We	Weber number

Greek symbols

μ	dynamic viscosity, kg m^{-1} s^{-1}
ν	kinematic viscosity, m^2s^{-1}
ρ	density, kg m^{-3}
φ	Volume fraction of the primary phase (phase 1)
λ	Volume fraction of the secondary phase (phase 2)
γ	Volume fraction of the third phase (phase 3)
k	curvature of interface
σ	interfacial tension coefficient, kg s^{-2}
ψ	stream function$\left(=-\int_{Y_0}^{Y} U\partial Y+\psi(X,Y_0)\right)$

Subscripts

L	Lighter fluid
H	Heavy fluid
M	Middle fluid

1. Introduction

Multiphase flows where two or more immiscible fluids exist simultaneously in a domain are ubiquitous in a wide range of industrial and natural processes including fluidized beds [1,2], tsunami propagation [3–5], droplet impact [6,7], sediment transport [8,9], landslides and impulse waves [10]. The utilization of numerical methodologies as a promising cost-effective alternatives to conventional experimental and theoretical approaches has received a great deal of attention during the last two decades [11]. However, the accurate tracking or capturing of the moving interfaces, together with the complex interface dynamics (i.e. coalescence or segregation) and discontinuous variations of material properties that frequently characterize such phenomena, impose tremendous challenges on numerical modelling [12]. Fundamentally, interface-resolved simulations of multiphase flows can be differentiated into two distinct categories according to the interface representation namely: (Ⅰ) interface-tracking, and (Ⅱ) interface-capturing methods [13,14]. With the former approach, the position of the material discontinuities is explicitly determined by a set of mobile particles attached to the interface (Lagrangian markers). Examples include Arbitrary-Lagrangian Eulerian (ALE) [15], front-tracking [16] and point-set method [17]. However, these models are computationally expensive and needs regular particle rearrangement (or re-meshing) especially when the interface is stretched or compressed [18]. Methods that fall in the second class are the Level-Set, (LS) [19] and the Volume-Of-Fluid (VOF) [20] in which an auxiliary scalar partial differential equation (PDE) is implicitly solved to represent the interface profile. Given the pros and cons of both methods, LS and VOF have been extensively applied to a broad range of engineering problems such as atomization and solidification [18,21], dam failure [22–24] and bubble rising [25,26]. However, the results of the Gibou et al. [27] showed that, although LS model can accurately compute the geometrical quantities of the interface (i.e. interface normal and curvature) using a smooth implicit Heaviside function, this model is typically plagued by mass conservation issues which in turn leads to a substantial loss of accuracy. On the other hand, Yin et al. [28] and Marić et al. [29] conducted comprehensive reviews on the last application of the Volume-Of-Fluid model and concluded that, although VOF model can intrinsically guarantee discrete mass conservation and is relatively simple to implement in practice, this model is characterized by some crucial drawbacks such as:

(1) unphysical growth of interface thickness arising from false-diffusion errors [30,31], (2) inaccuracy in estimating interface curvature [32,33], (3) unphysical pressure/velocity fluctuations around the material discontinuity [34,35] which can immensely jeopardize the reliability and consistency of the numerical solutions and render nonphysical flow physics, accordingly. During last decades, substantial research efforts have been devoted to address the aforementioned shortcomings.

Inspired by work of Boris and Book [36], in a pioneering works, Harten [37] and Leonard [38] introduced the notion of High resolution non-oscillatory differencing schemes to address the problem of interface smearing and suppress detrimental effects of numerical diffusion. They proposed two novel second-order bounded convection schemes so-called TVNI and SHARP based on the TVD (Total Variation Diminishing) [39] and NVD (Normalized Variable Diagram), and found that, monotone difference schemes can offer better iterative convergence properties in comparison with the classical unbounded oscillatory ones such as second-order Upwind (LUD), Central Differencing (CD), QUICK and Fromm [40], when applied to the implicit solution methods. Moreover, they pointed out that, the implementation of the hybrid non-linear flux-limiter schemes exhibit better resolution of steep gradients and discontinuities but at the expense of a higher computational cost due to the switching between different flux-limiter schemes especially when the interface orientation is tangential to the flow direction. Similar findings were also reported by Zhang et al. [31] who conducted a comprehensive literature survey on the various TVD schemes and highlighted that gradually-switching smooth flux-limiters can lead to the better convergence behavior compared to the piecewise linear limiter functions. From then on, various conservative differencing schemes were constructed by using the unique relationship between NVD and TVD constraints. Examples include SOUCUP [41],

MINMOD [37], SMART [42], TOPUS [43], HLPA [44], GAMMA [45], Van Leer [46], SMARTER and LPPA [30]. However, the results of Ubbink et al. [47] revealed that, the global order of these schemes are restricted to the second-order in any case. In addition to that, they are derived based on one-dimensional assumption which can hinder their further applications in multi-dimensional problems. To overcome this issue, they proposed a blended control-volume flux-limiter formulation named as "CICSAM" based on the Normalised Variable Diagram which switches smoothly between two high resolution schemes namely Hyper-C and Ultimate-Quickest (UQ). They claimed that, CICSAM is capable of preserving the integrity of the interface while reducing the diffusion errors. However, in the same context, Malgarinos et al. [48], Nguyen et al. [49], Wacławczyk et al. [50] questioned the capability of CICSAM scheme in handling large topological changes and stressed that the CICSAM scheme cannot satisfactory recover interface sharpness and is also prone to numerical smearing due to its inherent low order of accuracy. In order to mitigate the adverse effects of numerical diffusion and to cope with heterogeneity in physical properties, Garoosi et al. [51] proposed a novel third-order accurate flux-limiter function which guarantees boundedness condition while maintaining interface shape. They evaluated and tested the feasibility and accuracy of their scheme against a set of canonical test cases and showed that, the newly developed TVD function can successfully meet the completeness requirements for convective stability, convergence criteria, monotonicity and algorithmic simplicity. However, further assessment of performance and outcome is required prior to implementing/extending it to some intricate multi-fluid problems.

Referring to the second drawback related to the VOF model, Pozzetti et al. [52], Dianat et al. [53] and Zhang et al. [54] suggested the use of PIMPLE algorithm (PISO-SIMPLE algorithm available in OpenFOAM® platform) to circumvent the problem of velocity/pressure jump across the interface. However, since an additional iterative SIMPLE algorithm is incorporated into the standard PISO loop, this pressure-based solver seems not to be computationally efficient particularly when it will be extended to the three-dimensional real-life problems with large scale [55]. To remedy this deficiency, Garoosi et al. [51] proposed a novel hybrid semi-iterative PISOC algorithm by the combination of the classical PISO [56] and Two-step projection [57] models. Their results showed that, PISOC algorithm can appreciably remove the spurious pressure/velocity oscillations from fluid domain with affordable computational cost.

Finally, as stated before, the third challenge faced by VOF model is to determine the exact value of interface normal/curvature for the accurate enforcement of surface tension force. To tackle this problem, Youngs [58,59] introduced the first-order accurate interface reconstruction technique in the context of the PLIC concept and then successfully utilized for modelling of Rayleigh-Taylor Instability problem. However, despite its many uses and applications in both commercial and open source CFD softwares, the analytical investigation of Pilliod et al. [33] revealed that, Youngs' method cannot exactly reproduce all linear interface and is prone to fragment a smooth front. As an alternative approach, he proposed the ELVIRA technique for the reconstruction of interface and demonstrated that the method is second-order accurate on smooth interfaces. This technique was then coded and adopted by Garoosi et al. [51] for numerical investigation of multiphase flows with moving interfaces.

The above literature review clearly demonstrate that, the previous work of Garoosi et al. [51] systematically addressed three crucial shortcomings related to the interface-capturing VOF model. However, these improvements still need further verifications before being generalized to multi-fluid flows with high density contrast and surfactant. Based on the above explanation, the purpose of the present work is twofold: (1) to demonstrate the versatility of the enhanced VOF model in handling two- and three-phase flows, and (2) to introduce two novel benchmark problems for CFD validation. To accomplished this objectives, in the first stage of the current work, the validity and accuracy of the enhanced VOF model is further tested against the additional canonical test cases including draining of liquids from the storage tank (tank draining), single rising bubble, three-phase Rayleigh-Taylor Instability and dam-break flows over dry and wet beds. In the second stage, the verified VOF model will be employed to investigate two new challenging cases namely: merging of two rising bubbles with different densities and diameters, aiming to provide the state-of-the-art benchmark solutions and up-to-date data set for CFD validations. To the best of authors' knowledge, such challenging benchmark problems have not been reported in the literature. The simulated results are presented in forms of volume fraction and pressure contours and related interface profile.

2. Problem statement and governing equations

The geometrical configurations of physical models with associated boundary conditions are portrayed in Fig. 1. In the present work, the first six canonical problems (cases 1-6) are chosen to further verify the capability and versatility of the improved version of VOF model in dealing with the multi-fluid flow problems with low and high density contrasts whereas cases 7 and 8 as two new benchmark problems will be analyzed in details. The numerical analyses were carried out using FORTRAN 90 programming language where the Intel® Visual FORTRAN Compiler 19.0 was used for the compilation of the developed code. The governing equations (i.e. mass, momentum and volume fraction) for the Newtonian, laminar and incompressible multiphase flows in the Eulerian description can be written as follows [47,60]:

$$\frac{\partial \rho}{\partial t} + \frac{\partial \rho u}{\partial x} + \frac{\partial \rho v}{\partial y} = 0, \tag{1}$$

$$\frac{\partial \rho_m u}{\partial t}+\frac{\partial \rho_m uu}{\partial x}+\frac{\partial \rho_m vu}{\partial y}=-\frac{\partial p}{\partial x}+[\frac{\partial}{\partial x}\mu_m(\frac{\partial u}{\partial x})+\frac{\partial}{\partial y}\mu_m(\frac{\partial u}{\partial y})]+F_{ST} \tag{2}$$

$$\frac{\partial \rho_m v}{\partial t}+\frac{\partial \rho_m uv}{\partial x}+\frac{\partial \rho_m vv}{\partial y}=-\frac{\partial p}{\partial y}+[\frac{\partial}{\partial x}\mu_m(\frac{\partial v}{\partial x})+\frac{\partial}{\partial y}\mu_m(\frac{\partial v}{\partial y})]+\rho_m g+F_{ST} \tag{3}$$

$$\frac{\partial \varphi}{\partial t}+\frac{\partial \varphi u}{\partial x}+\frac{\partial \varphi v}{\partial y}+\nabla\cdot(\varphi(1-\varphi)\mathbf{u}_R)=0 \tag{4}$$

$$\frac{\partial \lambda}{\partial t}+\frac{\partial \lambda u}{\partial x}+\frac{\partial \lambda v}{\partial y}+\nabla\cdot(\lambda(1-\lambda)\mathbf{u}_R)=0 \tag{5}$$

$$\varphi+\lambda=1 \text{ or } \varphi+\lambda+\gamma=1 \tag{6}$$

where u, v, g, p and t denote the velocity components in 2D Cartesian coordinate system, gravity acceleration, pressure and time, respectively. ρ_m and μ_m are density and dynamic viscosity of the mixture which can be calculated through the φ-, λ- and γ-weighted average of phases in each computational cell as [61]:

$$\rho_m=\varphi\rho_1+(1-\varphi)\rho_2 \tag{7}$$

$$\mu_m=\varphi\mu_1+(1-\varphi)\mu_2 \tag{8}$$

$$\rho_m=\varphi\rho_1+\lambda\rho_2+(1-\lambda-\varphi)\rho_3 \tag{9}$$

$$\mu_m=\varphi\mu_1+\lambda\mu_2+(1-\lambda-\varphi)\mu_3 \tag{10}$$

In the above formulations, Eqs. (7)-(8) are adopted for the approximation of the density and viscosity of two-fluid flow problems whereas Eqs. (9) and (10) are used to predict the fluid properties in the three-phase problems with subscripts 1, 2 and 3 being reference fluid-components. The last term F_{ST} in Eqs. (2) and (3) stands for the surface tension force which is approximated based on the Continuum Surface Force (CSF) model proposed by Brackbill et al. [62] as:

$$F_{ST}=\sigma k\nabla\varphi \tag{11}$$

where σ denotes the surface tension coefficient between two phases and k represents the curvature of interface defined as [28]:

$$k = -\nabla \cdot \mathbf{n} = -\nabla \cdot (\frac{\nabla \varphi}{|\nabla \varphi|}) \tag{12}$$

$$\mathbf{n} = \frac{\vec{n}}{|\vec{n}|},\ \vec{n} = \nabla \varphi \tag{13}$$

where $\mathbf{n}$ indicates the interface unit normal vector which is pointing away from the interface. The third terms ($\nabla \cdot (\varphi(1-\varphi)\mathbf{u}_R)$ and $\nabla \cdot (\lambda(1-\lambda)\mathbf{u}_R)$) in the transport equations (i.e. Eqs. (4) and (5)) are known as the Artificial Compression Term (ACT) [63–65] which are non-zero in the close proximity of interface region owing to the existence of $\varphi(1-\varphi)$ and $\lambda(1-\lambda)$ terms. Note that, the additional ACT term has a tendency to preserve the interface sharpness especially when the flow is tangential to the interface. $\mathbf{u}_R$ is the compressive velocity which act perpendicular to the fluid interface and may be estimated based on maximum velocity magnitude as follows [66,67]:

$$\mathbf{u}_R = C_\varphi |\vec{u}| \mathbf{n} = C_\varphi |\vec{u}| \frac{\nabla \varphi}{|\nabla \varphi|} \tag{14}$$

The coefficient $C_\varphi = 0.5$ is the compression factor which controls the strength of interface compression and ranges from 1 to 2 dependent on the grid resolution [68–70].

3. Numerical methodology

The system of governing partial differential equations (Eqs. 1-5) are solved using finite volume method (FVM) on a staggered grid arrangement where no interpolation is required to estimate velocity components at the scalar cell faces which in turn results in the proper velocity-pressure coupling and total elimination of unphysical checkerboard pressure fluctuations [71]. Structured uniform mesh in *X* and *Y*-directions are utilized for all computations and the transient terms in the momentum and transport equations are treated implicitly using a second-order backward differencing scheme [72]. The diffusion terms in the Navier-Stokes equation is approximated by the second-order central differencing scheme while a third-order TVD upwinding scheme proposed by Garoosi et al. [51] is utilized for the discretisation of the convection terms in momentum and volume fraction equations. In order to enforce the conservation of mass in unsteady incompressible multiphase flows, the semi-iterative version of the improved PISO algorithm is applied for the treatment of the pressure-velocity coupling where two classical PISO [56] and Two-step projection (Chorin's model [57]) approaches are merged in the single hybrid algorithm (labelled hereafter as PISOC). Details regarding the solution procedure and derivation of the PISOC algorithm can be found in previous work of Garoosi et al. [51] (see also Appendix A) . To further enhance the stability and consistency of the numerical solutions, the second-order interface reconstruction technique (ELVIRA) pioneered by Pilliod et al. [33] is implemented for the estimation of the interface curvature and the enforcement of the surface tension force, accordingly.

4. Validation and verification

To verify the feasibility and robustness of the proposed VOF model in handling multiphase flows with sever interface deformation and fragmentation, six different challenging benchmark test cases are numerically reproduced in this section. The first, second and third canonical test cases are classical dam-break flows (cases 1 and 2) and tank draining (case 3) where owing to sudden collapse of liquid column and high density contrast between phases (water-air fluids), the hydrodynamic/hydraulic behavior of the free-surface flow is characterized by series of interface rupture and coalescence events. The fourth and fifth benchmark examples are three-phase

Rayleigh-Taylor Instability problems (case 4 and 5) where due to the low density ratio between phases and the appearance of Kelvin-Helmholtz instability within the computational domain, the fluid interface is likely to undergo sever distortion including twisting, flattening or even filamentation. The last benchmark problem (case 6) involves the study of classical bubble rising with high density and viscosity ratios where due to the existence of the surface tension force and development of the wake region, the phenomenon so-called bubble detachment with associated interface filamentation are likely to occur within the fluid domain. The obtained results are presented in separate subsections and discussed in details.

4.1.Dam-break flow over dry and wet beds (cases 1 & 2)

Transient evolution and hydrodynamic characteristics of dam-break flow over a horizontal dry and wet bed are analyzed in this subsection. As sketched in Fig. 1, the calculations in the first benchmark problem (case 1) are carried out in a prismatic rectangular flume with dimensional size of $D = 1.4m$ and $L = 1.61m$ where the water column ($g = 9.81ms^{-2}$, $\rho = 997\,kgm^{-3}$, $\mu = 855\times10^{-6} kg\, m^{-1}s^{-1}$) with initial width and depth of $W = H = 0.6\,m$ is stored on the left side of the reservoir. The rest of the enclosure is occupied by air ($\rho = 1.0\,kgm^{-3}, \mu = 184\times10^{-7} kg\ m^{-1}s^{-1}$) as a secondary phase and the effects of surface tension force ($\sigma = 0.071\,Kgs^{-2}$) are taken into consideration. The simulation is performed on the uniform grid resolution of 500×435 (in *x*- and *y*-directions) and the initial zero values are assigned for pressure and velocity across the whole channel ($p = 0, u = v = 0\,ms^{-1}$). The time histories of the water level height are monitored at three different sites ($l_1 = 0.3m$, $l_2 = 1.114m$ and $l_3 = 1.362m$) and pressure variations are recorded by two sensors installed on the downstream wall ($h_{R1} = 0.03m$ and $h_{R2} = 0.08m$). No-slip impermeable wall boundary conditions are imposed on all stationary walls and obtained results in terms of volume fraction and pressure contours are displayed in Fig. 2. The predicted results reveal that once the virtual lifting gate is removed, the standing water column descends downward under the gravity force and is promptly replaced by traveling wave, indicating the rapid conversion of the potential energy of the system into the kinetic one. As time progresses ($0 < T < 1.61$), the flooding wave freely propagates over the initially dry bed and elongates horizontally until it encounters the boundary layer of downstream wall approximately at time $T = 1.61$ where the first impact pressure and wave deflection occur ($P_{\max 1,R1} = 2.29$, $P_{\max 1,R2} = 1.44$). However, since the right wall is rigid and impermeable, the resultant impact wave starts to deviate upward and moves vertically along the rigid wall, leading to the formation of the ascending jet in that area. It is worth mentioning that, this stage is also accompanied by the emergence of semi-hydrostatic pressure distribution and stagnation point (or fluid trapping phenomenon) on the bottom-right corner of the flume which manifest themselves through an asymptotic reduction in the values of pressure load during the time period of $1.61 \le T \le 4.15$ (see also Fig. 3). As time proceeds, the intense upwelling jet grows in size and amplitude until the tip of the liquid jet reaches its maximum elevation at $Y = y/H \approx 2.0$ and $T = 3.2$ which is approximately twice the initial water level height at dam site. Similar finding was observed and documented by Colagrossi et al. [73] who numerically investigated the same benchmark problem but with different initial water depth. Later, due to restoring action of the gravity force, the up-rushing liquid jet is eventually flipped down and decelerated, leading to the creation of reverse plunging wave breaker with maximum wave crest height of $Y = y/H \approx 0.97$ which is nearly equals to the initial water level height at upstream region (compare two snapshots of the volume fraction contours at time instants of $T = 0.638$ and

$T = 4.707$). In addition, a close inspection of the pressure contours in Fig. 2 illustrates that during this period of evolution, the quasi-hydrostatic pressure zone expands to occupy larger part of the rolling wave which indicates that the main flow is primarily governed by transverse inertia force in *x*-direction. This phenomenon corresponds to the progressive augmentation in time histories of pressure variations during the period of $4.15 < T \leq 5.05$ (see also Fig. 3). Ultimately, the backward plunging breaker collapses obliquely onto the advancing water surface below and penetrates it, producing an egg-shaped air cushion structure and the second peak pressure ($P_{\max 2,R1} = 1.18$, $P_{\max 2,R2} = 1.09$) at $T = 5.05$. The position of shock pressure is also visible around the collapse site (see snapshot of the pressure contours at $T = 5.026$) which presumable results from the immersion of reflected jet. However, as mentioned before, the impact of the plunging wave on the wetted bed generates a new surge with moderate celerity which spurts from the free-surface of incoming dam-break wave and travels obliquely towards the upstream area, resulting in a strong air-water flow interaction with associated gas entrapment.

Comparison of the obtained results with experimental and numerical data of Lobovský et al. [74] and Sun et al. [75] are plotted in Fig. 3. The overall examination of the figure shows that, the snapshots of the free-surface profile at three different time instants together with the non-dimensional pressure variations predicted from the current work are in a satisfactory agreement with previously published data. Moreover, it is evident that the proposed model can effectively preserve the integrity and sharpness of the interface especially during the occurrence of the plunging breaker when flow-to-grid skewness is substantial. Thanks to the hybrid PISOC algorithm, the pressure field is totally free from the spurious fluctuations, which in turn confirms superiority of the proposed semi-iterative pressure-based model over the classical PISO and Two-step projection (Chorin's model) approaches in dealing with the highly non-linear incompressible fluid flows. Finally, it is worthwhile to mention that, the time histories of non-dimensional surge front location (X_{front}) and water column height at three different sections are presented in Fig. 3 as additional information which have not been reported in the literature.

The problem of dam break flow over the initially wet bed is considered and reproduced here as a second test case (case 2). This small-scale laboratory experiment was originally conducted by Jánosi et al. [76] and then numerically reproduced by Jonsson et al. [77], Ye et al. [78], Crespo et al. [79] and Gu et al. [80]. The configuration of the prototype experiment is sketched in Fig. 1. As it can be observed, the simulation is carried out in a prismatic rectangular duct with dimensional size of $D=0.3m$ and $L=1.2m$ where the rectangular water column ($g=9.81ms^{-2}$, $\rho=997\,kgm^{-3}$, $\mu=855\times10^{-6}kg\,m^{-1}s^{-1}$) with width and depth of $W=0.38m$ and $H=0.15m$ is connected to the downstream wet bed with initial water level height of $B=0.018m$. The rest of the channel is filled by air ($\rho=1kgm^{-3}, \mu=184\times10^{-7}kg\ m^{-1}s^{-1}$) as a secondary phase and the effects of surface tension force ($\sigma=0.071\,Kgs^{-2}$) are taken into account. The simulation is performed on the uniform grid resolution of 480×120 (in *x*- and *y*-directions) and the initial zero values are assigned for pressure and velocity fields ($p=0, u=v=0ms^{-1}$). The time variations of the free-surface profile are recorded at three different sections ($l_1=0.1m, l_2=0.5m$ and $l_3=0.9m$) and dynamic pressure variations on the bottom wall are monitored by three virtual sensors deployed at $l_1=0.1m, l_2=0.7m$ and $l_3=1.0m$. No-slip impermeable wall boundary conditions are imposed on all rigid walls and predicted results in forms of volume fraction and pressure fields are portrayed in Figs. 4 and 5. Generally, although the global hydrodynamic and morphologic behavior of dam failure processes over the dry and wet beds are relatively identical, there are substantial differences when they come to hydraulic jump and plunging jet formations

[81]. It is evident from Fig. 4 that, contrary to the previous benchmark problem, owing to the head water differences between the falling water and downstream wet deck, the shock wave in form of weak ascending jet is immediately appeared at the junction of the upstream and the downstream areas and projected obliquely over the underlying wet bed as its kinetic energy increases. As time goes on, the front face of the stress wave steepens and becomes gradually horizontal. In these circumstances, due to the influence of the gravity force, the vertical celerity of the advancing wave decreases and consequently the resultant plunging breaking jet starts to fall down and hits the undisturbed water surface at T=2.205 and $x \approx 0.69m$, leading to the emergence of the entrapped cavity (air tube) with a visibly large radius of curvature. This phenomenon corresponds to the rapid augmentation in the pressure time history ($P_{\max 1, l2} = 0.326$) recorded by sensor 2 installed at $l_2 = 0.7m$ (see also Fig. 5). However, the remaining portion of the kinetic energy of the system causes the overturning jet to rebound from the wet bed as a new ascending wave and travels downstream. As expected, this mechanism results in the creation of the second large air-cushion structure at T=3.52 and $x \approx 0.985m$ with pronounced concentrations of vorticity. A third plunging action can also been observed during the time period of $3.528 \le T \le 4.491$ but at a much smaller scale. The comparison of the obtained results with previous works of Jánosi et al. [76] and Gu et al. [80] in Fig. 5 shows that, there is an excellent agreement between outcomes of the current study and published experimental data. However, as anticipated, it is evident that, the conventional VOF-LS model fails to predict the main features of the process which can be attributed to two aforementioned shortcomings associated with interface-capturing methods. On the other hand, the zoomed-in views of the interface in Fig. 5 reveal that, the proposed VOF model successfully alleviates the detrimental effects of numerical diffusion, thereby preserving the sharpness of the interface. Thanks to the

proposed TVD convection scheme, the thickness of the interface is efficiently controlled and limited to the 2-3 grid spacing and morphological changes of the dynamic process are well reproduced. Finally, similar to the previous test case, the time histories of the water level height and pressure variations at three different sections/points are presented in Fig. 5 which have not been reported in published literature.

4.2.Tank draining problem (case 3)

The temporal evolution and hydraulic characteristics of liquid draining from a vessel is examined in this subsection. The initial configuration of the system is similar to numerical work of Ghadampour et al. [82] where a quiescent column of water ($g = 9.81 ms^{-2}$, $\rho = 997\, kgm^{-3}$, $\mu = 855\times10^{-6} kg\, m^{-1}s^{-1}$) with width and height of $W = H = 0.15m$ is initially confined in the left side of the square reservoir with physical dimension of $L = D = 0.35m$. Similar to the previous test case, the rest of the reservoir is filled with air ($\rho = 1kgm^{-3}, \mu = 184\times10^{-7} kg\ m^{-1}s^{-1}$) and the effects of the surface tension force ($\sigma = 0.071\, Kgs^{-2}$) are taken into account. The simulation is performed on uniform grid size of $\Delta x = \Delta y = 0.001m$ (352×352 mesh resolution) and no-slip boundary condition of zero velocity is imposed on all rigid walls. In order to induce the discharging process of water storage tank (partial breach dam-break flow), the stationary rigid wall and drain port with dimensions of $R = 0.58L = 0.203m$ and $S = 0.1L = 0.035m$ are installed at a distance of $x = 0.15m$ from the upstream boundary wall. Qualitatively, topological characteristics and hydrodynamic peculiarities of the tank draining are analogous to the former benchmark problem where conversion of potential energy into kinetic one occurs immediately once the sluice gate is opened. It is evident from Fig. 6 that, after the removal of the submerged gate, the stored water starts flowing through the breach and progressively spread over the flume bed until the flood wave impacts the opposite wall. During this process, the water level height at the storage site gradually decreases which implies that the fluid flow in upstream of a vertical sluice gate is subcritical. On the other hand, the appearance of a hydraulic jump at $0.485 \le T \le 1.536$ conveys that the fluid flow in the downstream is supercritical and the discharge may be determined by the upstream water depth and the gate opening [83]. However, after the impingement of the wave front onto the right wall, the surge wave changes its direction and propagates vertically until the wave crest reaches the its maximum position ($Y = y/H \approx 2.0$) at $T \approx 3.153$. As anticipated, this mechanism leads to the development of the pressure shock region ($P_{\max 1} = 1.67\,m$) on the bottom-right corner of the enclosure at $T = 1.21$ which is monitored by sensors 1 deployed on the right wall ($h_{R1} = 0.0\,m$, see also Fig. 7). As time goes on, due to the retarding effects of gravity force, the newly generated sharp-crested wave (jet-like structure) starts to evolve into the plunging breaker which ultimately hits and immerses into the oncoming water discharge, leading to the establishment of an egg-shaped air cushion structure and second impact pressure ($P_{\max,R1} = 1.420$, $P_{\max,R2} = 1.056$ and $P_{\max,R3} = 0.491$) at $T = 4.528$. From the spatial anatomy of the stress wave at $T = 4.528$ one can deduce that, due to the backward movement of the impinging jet and forward momentum of the water discharge, a clockwise rotating eddy may be developed within the air pocket. This flow pattern was originally termed "*plunging vortex*" by Basco [84] in the context of wave breaking. Another key feature of this interaction is the axial meeting of these two water masses which leads to the strong impulse wave and large pressure gradients on the flume floor at $x = 0.24m$ (see pressure contour at $T = 4.528$). Note that, from the hydraulics point of the view, the impingement zone of a plunging jet is referred to as the *submerged hydraulic jump* region where mechanic energy (kinetic energy) of the slanting jet is irreversibly dissipated into the pressure shock [85].

Nevertheless, the residual or small excess momentum of the system with the aid of advancing plunging vortex cause the submerged jet to rebound from the underlying wetted bed and migrates towards the sluice gate where due to the integrated interaction of pseudo-plunging breaker and rigid gate, the third impact pressure and second air entrapment (air cavity structure) take place.

Qualitative comparison of the obtained results with numerical work of Ghadampour et al. [82] in Fig. 7 shows that, the early stage of the tank draining process is well predicted by the enhanced VOF model. As can be seen from the results, the thickness and sharpness of the interface are well controlled and preserved during the simulation which vividly proves the capability of the proposed modifications in capturing steep gradients and retaining the boundedness of the volume fraction between $0 \le \varphi \le 1$. Furthermore, it is evident that, the pressure field is satisfactory smoothed and the propagation of numerical diffusion arising from flow-to-grid skewness is effectively attenuated by the proposed third-order bounded TVD convection scheme. However, due to lack of essential information concerning tank draining problem in Ref [82], the pressure time history at three different marked points on the right (h_{Ri}) and left (h_{Li}) walls of the enclosure together with the time histories of wave front location (X_{front}) and water level heights at two different sections ($l_1 = 0.06m$ and $l_2 = 0.26m$) are provided as supplementary data on present problem which may be utilized by scholars for assessment and validation of various CFD tools. However, before ending this section, it should be noted that, the small peak in the time histories of pressure variations recorded by sensors $h_{L1} = 0.0m$, $h_{L2} = 0.05m$ $h_{L3} = 0.1m$ on the left wall can be attributed to the assigning initial zero pressure instead of imposing pre-known hydrostatic pressure value ($P_{Initial} = \rho g H$). This statement implies that, the pressure field is progressively determined through the PISOC algorithm during the simulation.

4.3.Three-phase Rayleigh-Taylor Instability (cases 4 and 5)

The initial growth and tortuous evolution of three-phase Rayleigh-Taylor Instability problem is investigated in this subsection. The benchmark test cases were originally introduced by Garoosi et al. [86] in the context of the Lagrangian description by means of the Moving Particle Semi-implicit (MPS) method. As sketched in Fig. 1, three immiscible incompressible viscous fluids with nominal densities of $\rho_H = 4.0$, $\rho_M = 2.0$ and $\rho_L = 1.0$ are sequentially positioned at the top, middle, and bottom parts of the enclosure, respectively. All fluids have identical kinematic viscosities ($\nu_H = \nu_H = \nu_H = 0.01$). The simulations are conducted in the computational domain with size of $\left[0, H\right] \times \left[0, 3H\right]$ where $H = 1m$ denotes the width of the enclosure. The initial positions of interfaces between each pair of the fluids in configuration of case 4 are set to $y_1 = 1.0 + 0.1 \times \cos(2\pi x)$ and $y_2 = 2.0 + 0.1 \times \cos(2\pi x)$ whereas the interfaces in case 5 are initialized as $y_1 = 1.0 + 0.1 \times \cos(2\pi x)$ and $y_2 = 2.0 - 0.1 \times \cos(2\pi x)$, respectively. The instability in both cases is governed by non-dimensional Reynolds and Atwood numbers equal to $\mathrm{Re} = \rho_H H \sqrt{gH} / \mu_H = 420$ and $At = (\rho_H - \rho_L)/(\rho_H + \rho_L) = 3/5$, respectively. The mesh resolution of 300×900 is chosen for both cases and the effects of surface tension force are neglected. However, contrary to the previous test case, since three distinct fluids are engaged in cases 4 and 5, Eqs. (4) and (5) are utilized to calculate the volume fractions of dense (φ) and middle (λ) fluids, respectively while the formula ($\varphi + \lambda + \gamma = 1$) in Eq. (6) is employed to estimate the volume fraction of the lighter fluid. Figs. 8 and 9 exhibit the time evolution of the density contours in cases 4 and 5. As displayed in Fig. 8, in the early stages of the RTI development, the heavy fluid (ρ_H) on top in case 4 starts to penetrate into the less-dense phase (ρ_M), meanwhile the middle fluid rises up from the sides of the enclosure in the form of plumelike structure. However, since both interfaces in case 4 are perturbed in the same directions, this course of the event also occurs between middle (ρ_M) and lighter (ρ_L) fluids. Hence, two pairs of bubble-spike structures with associated vortex sheets are established within the enclosure. Scrutiny of the figure illustrates that, during the early stages of the evolution ($0 \le T \le 1.575$), the harmonic growth of the fluid interfaces remains symmetrical with respect to the center of the enclosure which indicates that the instability still follows the linear theory [87]. However, as expected after a finite time, due to the low density disparity between phases, the main flow becomes unstable to the Kelvin-Helmholtz shear instability which causes the initial disturbance to lose its symmetry feature and enter the weakly nonlinear mode ($1.575 < T \le 2.520$) [88]. As time goes on, the formation of the spikes gets more prominent and intensity of the Kelvin's circulation increases. This intermediate stage of the development ($2.520 < T \le 3.150$) is also accompanied by the broadening of vortex shedding in the wake of spike which manifest itself through inward folding of the interface. As the instability grows further ($3.150 < T \le 4.095$), the rising wings of the lighter fluid start to embrace the falling spike of the denser fluid, resulting in the appearance of the tulip-shaped structure (or harpoon-like pattern). In this circumstance, the tails of the roll-ups evolve into the complicated pattern and consequently the fluid flow enters the fully non-linear regime where the corresponding contraction of the dense fluid alters the pattern into the needle-shaped spike. The surrounded spike keeps moving downward until it reaches the boundary layer of the bottom wall, giving rise to the substantial and sharp distortion of the interface with pronounced concentrations of vorticity. Inspection of the results in Fig. 8 also reveals that, the total displacement of the advanced bubble (lighter fluid) is considerably lower than that of the falling fluid. This finding may be attributed to the existence of some secondary eddies near the tips of the needle-shaped spike and due to the long horizontal distance between the primary spike and vertical walls of the container where no-slip velocity boundary condition is imposed.

However, Fig. 9 illustrates that by altering the direction of the upper cosinusoidal perturbation from $y_2 = 2.0 + 0.1 \times \cos(2\pi x)$ to $y_2 = 2.0 - 0.1 \times \cos(2\pi x)$, a different scenario appears within the container. It is evident that, since the interfaces in case 5 are disturbed in the opposite directions, at the early stages of the evolution ($0 \le T \le 2.520$), the middle fluid starts to penetrate simultaneously into the adjacent heavy and lighter fluids whereas the edges of the disturbed interfaces move radially towards the central zone of the enclosure to fulfill the need for the mass conservation. As the current progresses further ($2.520 < T \le 3.570$), the flow resistance of the lighter and denser fluids becomes important which causes the sides of the medium phase to roll-up and amalgamate into the unsteady swirling flow (vortex shedding). As stated before, this flow pattern is commonly cited as the onset of the Kelvin-Helmholtz Instability (KHI), which denotes the presence of the shear force in the rear of the spikes. As the simulation time proceeds ($3.570 < T \le 5.250$), the motion of the tips of a spikes slows down and interfaces undergo significant deformation. It can be seen from Fig. 9 that, during this process, the rising sheet plumes (lighter fluid, ρ_L) start to bifurcate and cover the falling dense fluid (ρ_H), forming a heart-like structure within the enclosure. In fact, the creation of the heart-like structure (Pitchfork bifurcation phenomenon [89]) and its expansion/broadening in the *x*-direction at the central portion of the fluid domain, are the signs of the fluid entrapment phenomenon and development of the quasi stagnation point which causes the falling liquid to get stuck in that region.

Qualitative and quantitative comparison in Fig. 10 demonstrate excellent agreement between the results of the present Eulerian VOF model with the data of Lagrangian MPS simulations [86].

More precisely, it is evident that, the bubble-spike structures in both cases alongside the maximum and minimum positions of the dense and lighter fluids are satisfactory reproduced and predicted using the enhanced VOF method. However, the small differences between two results can be attributed to the nature of the two models to address the problem of physical discontinuities in the multiphase flow problems. Another reason for such a discrepancy can be traced back to the order of accuracy of the numerical schemes implemented for the discretization of the governing equations.

4.4. Single rising bubble (case 6)

To further assess the accuracy and consistency of the improved VOF model in solving multiphase flows with high density contrast, the numerical simulation of the single bubble rising in quiescent liquid is considered here as a last benchmark problem. This canonical test case was originally introduced by Sussman et al. [19] and was then adopted by Almasi et al. [90], Kruisbrink et al. [91] and Zainali et al. [92] to check the performance of Smoothed particle hydrodynamics (SPH) method in dealing with the multi-fluid flows. Fig. 1 illustrates a schematic sketch corresponding to the initial setup of the problem where a circular bubble with density and viscosity of $\rho_L = 1.0\,Kgm^{-3}$ and $\mu_L = 1.106\,Kgm^{-1}s^{-1}$ is located at $[1.5H, 1H]$ where $H = 2R_0 = 1m$ represents the initial diameter of the bubble. The calculations are performed in a rectangular duct $[3H, 5H]$ filled with water as a secondary phase ($\rho_H = 1000.0\,Kgm^{-3}$ and $\mu_H = 3.130\,Kgm^{-1}s^{-1}$). The pertinent parameters for this canonical test case are density ratio $\rho_H / \rho_L = 1000$, viscosity ratio $\mu_H / \mu_L = 2.828$, Reynolds ($\mathrm{Re} = \rho_H 2R\sqrt{2gR} / \mu_H = 1000$) and Bond ($Bo = \rho_H g(2R)^2 / \sigma = 200$) numbers with $g = 9.8\,ms^{-2}$ stands for the acceleration of gravity. No-slip boundary condition ($\mathbf{u} = 0$) is applied on all rigid walls and the effects of surface tension force ($\sigma = 49\ Kgs^{-2}$) is taken into account. The uniform grid size of 450×750 is used for the simulation and obtained results in terms of volume fraction field with selected pressure contours are depicted in Fig. 11. Generally, the morphology and dynamics behavior of the rising bubble strongly depend on the magnitudes of the Reynolds and Bond numbers such that high surface tension (or low Bond number) and viscous (low Reynolds number) forces prevent the bubble from twisting, and tend to keep the bubble circular in shape , accordingly [93]. As seen from the figure, due to the existence of density gradient, the stationary bubble rises up under the action of buoyancy force while the water descends downward following the direction of gravity in the close proximity of the vertical walls, producing a pair of vortex rings behind the gas phase ($0 \le T \le 1.062$). This mechanism causes the bubble shape undergoes moderate dynamical change to form the well-known apple-like structure as documented by Hysing et al. [94]. As time passes ($1.062 < T \le 3.514$), the downwilling water motion with the aid of unsteady vortex shedding begin to squeeze the bubble which results in the formation of the horseshoe-shaped structure within the container. Once the bubble is pierced from the center, the inertial force acting on the bubble decreases and consequently the surface tension force which is more pronounced in regions with high interface curvature starts to play its role and subsequently tear the main body. In this circumstance ($3.514 < T \le 5.312$), the air bubble broadens, and the horseshoe shape eventually splits into three main segments. This stage may be referred to as the "*quasi terminal condition*" describing the morphology of a rising bubble where the piercing phenomenon, detachment of two satellite bubbles, and reduction in bubble velocity are come to pass sequentially in a short period of time [95]. However, as time progressed, the shape of the bubble becomes more stable and flatter which signifies that the unsteady process starts to reach its terminal velocity and hemispherical state where all relevant forces such as drag, gravity, surface tension, buoyancy and viscosity are in hydraulic equilibrium. This assertion is well supported by profiles of the interface positions plotted in Fig. 12 where due to the existence of the weak fluid circulation and wake shedding, the minimum location of the two daughter bubbles remains almost unchanged during the period time of $5.312 < T \leq 8.854$.

Coming to the comparison of the global characteristics of the bubble rising in Fig. 12, there is satisfactory agreement between results of present work and those reported by Almasi et al. [90], Kruisbrink et al. [91]. Moreover, the smoothness of the interface in the zoomed-in view of the grid near the trailing edge of the main bubble confirms the capability of the TVD convection scheme in capturing steep gradients without generating spurious oscillations or smearing. Finally, the minimum and maximum positions of the bubble versus non-dimensional time are also provided in Fig. 12 as additional information which may be used by scholars for validation/verification purposes.

5. Results and discussion

In the previous section, the accuracy and versatility of the enhanced version of the VOF model proposed by Garoosi et al. [51] were further verified against a series of challenging multi-fluid flow problems. However, from the numerical viewpoint, validation of CFD codes is of the great significant and has become a crucial part of the modelling process. As the number of users and programmers increases, the need for new benchmark solutions has received a great deal of attention by scientific community. Thus, at this stage, the verified VOF model will be employed to examine and analyze two new multiphase problems namely merging of two rising bubbles with different densities and diameters. The newly introduced benchmark solutions in the scope of multifluid flows can provide a reliable dataset for validation of numerical models and shed more light on the coalescence process of the rising bubbles.

5.1. Merging of two rising bubbles with different densities and diameters (cases 7 & 8)

The configurations of two new benchmark solutions are depicted in Fig. 1. As can be seen, the calculations in both cases are performed in a rectangular container with size of $[H, 2.2H]$ where $H = 1m$ represents the width of the enclosure. The enclosure is filled with heavy fluid with nominal density and viscosity of $\rho_H = 1000\,Kgm^{-3}$ and $\mu_H = 20\,Kgm^{-1}s^{-1}$ where two circular bubbles with physical properties of $\rho_M = 500Kgm^{-3}$, $\rho_L = 250Kgm^{-3}$, $\mu_M = 10\,Kgm^{-1}s^{-1}$ and $\mu_L = 5\,Kgm^{-1}s^{-1}$ are located at $[0.5m, 0.5m]$ and $[0.5m, 1.1m]$, respectively. The subscripts *H*, *M* and *L* stand for the three immiscible Newtonian fluids namely Heavy, Middle and Lighter, respectively. The initial diameters of two bubbles in case 7 are set as $R_1 = 0.2\,m$ and $R_2 = 0.3\,m$ whereas these values in case 8 are $R_1 = 0.3\,m$ and $R_2 = 0.2\,m$. The morphological evolution and hydrodynamic characteristics of the problems under consideration is governed by Reynolds and Froude numbers defined as $\mathrm{Re} = (2R_{\max})U_0/\upsilon_H = \sqrt{g}\,(2R_{\max})^{3/2}/\upsilon_H = 90$ and $Fr = U_0/\sqrt{g2R_{\max}} = 1.0$ where υ_H , U_0 and $R_{\max}$ denote kinematic viscosity ($\nu_H = \nu_H = \nu_H = 0.02$), reference velocity and maximum radius of the bubbles within the computational domain ($R_{\max} = 0.3\,m$). Inspired by works of Pan et al. [96] and Zhao et al. [97], in order to reach sever topological changes, the effects of surface tension force are not taken into consideration ($\sigma = 0$). The simulations are carried out on uniform distributed grid of 350×770 and no-slip boundary condition ($\vec{\mathbf{u}} = 0$) is imposed on all rigid walls. All working fluid including dense liquid (*H*) and bubbles (*M*, *L*) are assumed to be stationary at the initial state ($p = 0, \mathbf{u} = 0$

). The shape evolution mechanism of rising bubbles in a quiescent liquid with corresponding velocity contours are portrayed in Figs. 13-16. Generally, from the wave theory point of the view, the dynamic behavior of the rising bubble in a stagnant Newtonian liquid subjected to the gravitational acceleration can be divided into three distinct stages namely: (1) linear stage where the buoyancy force is dominant and fluid flow is characterized by the development of two primary vortices, (2) weakly or quasi-linear stage where the bubble motion decelerates and the resistance drag by the surrounding liquid becomes comparable by the buoyancy force, and (3) fully non-linear stage where the final shape of the bubble is controlled and limited by viscous drag and transport phenomenon starts to obey the Stokes law [98]. The snapshots of bubbles shapes at six different time instants in Figs. 13-16 illustrate that, in early stages of impulsive motion ($0 \leq T \leq 0.7$), the buoyancy force induced by the density gradients causes both bubbles in cases 7 and 8 to travel upward while the dense fluid sinks downward in vicinity of the vertical walls, leading to the development of a pair of counter-rotating eddies at the sides of the bubbles. The corresponded velocity contours in Figs. 14 and 15 reveal that as time elapses ($0.7 < T \leq 1.5$), due to lower flow resistance drag, the flow acceleration and magnitude of the vertical velocity are intensified. This mechanism is accompanied by the invigoration of the downward jet current of the surrounding liquid beneath the leading bubbles, which in turn causes the primary vortices to move towards the region behind the leading bubbles, promoting the emergence of the prolate shape. At this stage, the formation of the wake region between two bubbles becomes more prominent and consequently some secondary vortices are appeared inside the bubbles. After a fast acceleration, during the period of $1.5 < T \leq 2.5$, owing to the enhancement in the friction drag and shear force at the poles of the bubbles, the motion of the fluids flow slows down and the upper bubble in both cases begins to transform into the shape of a dimpled ellipsoidal-cap. It is constantly perceived that, the well-developed vortices encourage the leading bubbles to elongate longitudinally and envelop the lower bubbles. In these circumstances, due to the shielding effects of the wake flow on rear of the leading bubbles (*M*), the trailing bubbles (*L*) undergo sever deformation and start to be swallowed by the primary bubbles. It can be seen from Figs. 14 and 15 that, in the later rising moments ($2.5 < T \leq 5.5$) where the buoyancy effects are less important and viscous force is leading the fluid flow, the magnitude of the non-dimensional velocity components remains almost unaltered. This physical model is the strong indication of the onset of the terminal condition and non-linearity within the fluid domain. It is evident that at this stage, the merged bubbles in both cases move with their constant velocity while deforming into the complex patterns. However, as pointed out before, if the effects of surface tension force were considered, the distortion of the bubbles shapes would become much less significant than the results obtained in Fig. 13.

The time histories of the maximum positions of the bubbles fronts are displayed in Fig. 16. The close inspection of the figure shows that, although the global variations of the interfaces profiles in both cases are relatively similar and follow the general trend of the curves, the coalescence time is slightly different. It can be seen that, in case 8 the tips of the leading and trailing bubbles meet each other at $T \approx 4.4$ while this course of event occurs at $T \approx 5.5$. This behavior can be partially originated from the stronger wake region generated in case 8 which causes the trailing bubble to rise faster compared to the one in case 7. Another reason behind this behavior can be attributed to the larger diameter of the lower bubble in case 8 which in turn leads to the stronger buoyancy force and lower shear force at the beginning of the evolution. This assertion is well supported by Figs. 14 and 15 where the maximum vertical velocity in the entire evolution in case 8 is considerably higher than that of case 7. In fact, these observations suggest that, the diameter and density of the leading and trailing bubbles have significant impact on the coalescence process and morphological characteristics of dual bubbles rising phenomenon.

6. Conclusions

In the present work, the accuracy and stability of an enhanced version of the Volume-Of-Fluid (VOF) model proposed by Garoosi et al. [51] are further tested against a series of challenging benchmark cases including draining of liquids from the storage tank (tank draining), single rising bubble, three-phase Rayleigh-Taylor Instability and dam-break flows over dry and wet beds. In the second part of the study, the verified VOF model is adopted to examine and analyze the transient evolution of two rising bubbles with different densities and diameters, aiming to establish the state-of-the-art benchmark solutions and up-to-date dataset for the verification and validation of CFD codes. The results of the numerical analysis led to the following conclusions:

- It is found that, the enhanced VOF model allows accurate and consistent predictions of non-linear free-surface flows involving plunging wave breaking, large slamming events, impact pressure and interface rupture/coalescence.
- The results show that, the sharpness of the interface can be successfully preserved by implementing third-order TVD bounded convection scheme.
- The obtained results show that, the third-order TVD bounded convection scheme can efficiently alleviate the numerical diffusion, thereby eliminating interface smearing.
- Through the numerical modelling of the three-phase Rayleigh-Taylor Instability, it is found that, the enhanced VOF model is capable of resolving multi-fluid flows with sever topological changes in comparison with Lgrangian mesh-free particle model (MPS).

- It is found that, the implementation of the hybrid PISOC algorithm can efficiently stabilize the numerical solutions and provide smoother pressure distribution in terms of both space and time.
- The results of the single bubble rising with high density ratio vividly confirm that, the proposed numerical approach can successfully address the problem of physical discontinuities particularly when flow-to-grid skewness is substantial.
- The results of merging of two rising bubbles with different densities illustrate that, the enhanced VOF model is capable of handling non-linear multi-fluid flows with large deformation and twisting
- The numerical simulation of buoyancy-driven merging of two bubbles with different densities reveal that, the initial diameters of the leading and trailing bubbles have notable impact on the coalescence process and terminal bubbles shape.
- It is found that, in the problem of buoyancy-driven merging of two bubbles, the shape and deformation of the lower bubble are significantly influenced by the diameter and wake of the upper bubble.

Supplementary material

In order to provide a comprehensive understanding of simulated benchmark problems, seven different video files associated with cases 1 to 6 are provided as supplementary material.

Declaration of Competing Interest

The authors declare that they have no known competing financial interests or personal relationships that could have appeared to influence the work reported in this paper.

CRediT authorship contribution statement

Faroogh Garoosi: Conceptualization, Methodology, FORTRAN Code development, Validation, Visualization, Writing-Original Draft.

Tarek Merabtene: Investigation, Validation, Writing-Review & Editing.

Tew-Fik Mahdi: Supervision, Funding acquisition, Validation, Writing-Review & Editing.

Acknowledgment

This research was funded, in part, by a National Science and Engineering Research Council (NSERC) Discovery Grant for the co-author Tew-Fik Mahdi, application No: RGPIN-2021-03272.

Appendix A (Hybrid PISO-Chorin algorithm for solving Pressure-Poisson equation)

A methodology for derivation of the hybrid PISOC algorithm which is the hybrid version of the standard PISO algorithm [56] and Chorin's model (two-step projection method) [57] is elaborated along this appendix. The PISOC algorithm was originally pioneered by Garoosi et al. [51] for decoupling of velocity and pressure in Navier-Stokes equations on the staggered grid arrangement, aiming to eliminate numerical oscillation from the computational domain in incompressible multiphase flows and to speed up convergence rate of implicit iteration process. As outlined in section 3, the convection terms in the governing equations are discretized using the third-order TVD bounded scheme while the second-order central differencing scheme is applied for the treatment of the diffusion terms. Meanwhile, the pressure gradient term is approximated by means of the linear interpolation between two immediate nodes located on the momentum cell faces [71]. By implementing the above differencing schemes, a finite volume discretization of the momentum equations can be expressed in the form of a linear algebraic equation as:

$$a_{ip}\mathbf{u}_p = \sum a_{np}\mathbf{u}_{np} + S_u + S_t - A_p(p_p - p_{np}) \tag{A1}$$

where the subscript *nb* represent the neighboring velocity nodes and S_u is the volumetric source term. a_{ip} and a_{np} are the diagonal and neighbour coefficients which represents the implicit form of the convection and diffusion variables together with the transient term of $\partial\rho\mathbf{u}/\partial t$. As stated before, in order to ensure second-order temporal accuracy of the numerical simulation, the *three-time-levels* scheme proposed by Kim et al. [72] is utilized for discretization of the transient term as:

$$\frac{\partial\rho\mathbf{u}}{\partial t} = \frac{3(\rho\mathbf{u})_p^{n+1} - 4(\rho\mathbf{u})_p^{n} + (\rho\mathbf{u})_p^{n-1}}{2\Delta t} \tag{A2}$$

By substituting Eq. (A2) into Eq. (A1), the central coefficient a_{ip} and source term S_t for the transient flow can be written as:

$$a_{ip} = a_p + \frac{3\rho_p^{n+1}}{2\Delta t}\Delta x\Delta y \tag{A3}$$

$$S_t = \frac{4(\rho\mathbf{u})_p^{n} - (\rho\mathbf{u})_p^{n-1}}{2\Delta t}\Delta x\Delta y \tag{A4}$$

where a_p is the central coefficient arising from the discretization of the linearized steady-state Navier-Stokes equations (for more details see previous works of Tuković et al. [99]). To initiate the PISOC algorithm and to compute the coefficients and constant terms in the momentum discrete equation, the initial guessed value of $\mathbf{u}^*$ is assigned for velocity components. Ideally, the discretized momentum equations based on the guessed flow variables and correct pressure distribution (p^{n+1}) can fulfill both momentum and mass laws as [71]:

$$\mathbf{u}_p^{n+1} = \frac{\sum a_{np}\mathbf{u}_{np}^{*} + S_u + S_t}{a_{ip}} - \frac{A_p(p_p^{n+1} - p_{np}^{n+1})}{a_{ip}} \tag{A5}$$

It should be noted that, at this stage, all constant coefficients namely a_{np}, a_{ip} and A_p are evaluated using the initial guess, hence the terminology "*operator splitting*" [100]. By introducing the pseudo velocity ($\mathbf{u}$) into the methodology and eliminating the pressure gradient term from Eq. (A5), the first predictor-corrector step of the algorithm related to the Chorin's model (two-step projection model) can be accomplished as [101]:

$$\mathbf{u} = \frac{\sum a_{np}\mathbf{u}_{np}^{*} + S_u + S_t}{a_{ip}} \tag{A6}$$

$$\mathbf{u}_p^{n+1} = \mathbf{u} - \frac{2d_{ip}(p_p^{n+1} - p_{np}^{n+1})}{3} \tag{A7}$$

where $d_{ip} = A_p / a_{ip}$. By substituting Eq. (A8) into the following discretised continuity equation [102]:

$$[(\rho uA)_e - (\rho uA)_w] + [(\rho vA)_n - (\rho vA)_s] = 0 \tag{A8}$$

The following PPE equation can be obtained:

$$\begin{aligned}
&a_{i,j}P_{i,j}^{n+1} = a_{i+1,j}P_{i+1,j}^{n+1} + a_{i-1,j}P_{i-1,j}^{n+1} + a_{i,j+1}P_{i,j+1}^{n+1} + a_{i,j-1}P_{i,j-1}^{n+1} + \frac{3}{2}b_{i,j} - \frac{3}{2}\left(\frac{3\rho_p^{n+1} - 4\rho_p^{n} + \rho_p^{n-1}}{2\Delta t\rho_p^{n+1}}\Delta x\Delta y\right) \\
&a_{i,j} = a_{i+1,j} + a_{i-1,j} + a_{i,j+1} + a_{i,j-1} \\
&a_{i+1,j} = d_{i+1,j}\Delta y, \quad a_{i-1,j} = d_{i,j}\Delta y \\
&a_{i,j+1} = d_{i,j+1}\Delta x, \quad a_{i,j-1} = d_{i,j}\Delta x \\
&b_{i,j} = u_{i,j}\Delta y - u_{i+1,j}\Delta y + \hat{v}_{i,j}\Delta x - \hat{v}_{i,j+1}\Delta x
\end{aligned} \tag{A9}$$

where $b_{i,j}$ stands for the mass imbalance arising from the pseudo velocities. Once the pressure distribution is computed, the pseudo velocity field can be modified using Eq. (A7). At this stage, it is important to note that, contrary to the fully-iterative version of PISO or PIMPLE algorithm, in order to achieve some prescribed level of accuracy, the iteration process is only applied to Eq.

(A9) rather than extending it throughout the calculations, making the proposed PISOC algorithm more computationally efficient in comparison with traditional SIMPLE, SIMPLER, SIMPLEC, PISO and PIMPLE algorithms [55]. Note that, Eqs. (A1) to (A9) are part of the standard Chorin's model and also correspond to the SIMPLER algorithm [71].

To initiate the second part of the methodology related to the PISO algorithm, one can assume that, the pressure and velocity values predicted from the previous stage still cannot satisfy the conservation of mass after a prescribed number of iterations applied on Eq. (9). Thus, the superscripts of these variables (p^{n+1}, u^{n+1}) are replaced by (p^{*}, u^{**}). By substituting the semi-corrected values of p^{*} and u^{**} into the Eq. (A1), the discrete momentum equation for the current time step may be written as:

$$a_{ip}\mathbf{u}_{P}^{**} = \sum a_{np}\mathbf{u}_{np}^{**} + S_u + S_t - A_p(p_p^{*} - p_{np}^{*}) \tag{A10}$$

where $\mathbf{u}^{**}$ stands for the updated (modified) velocity field. However, by subtracting Eq. (A10) from (A1) and introducing the incremental pressure (p') and velocity variables ($\mathbf{u}'$), the following formulations can be achieved:

$$a_{ip}(\mathbf{u}_p - \mathbf{u}_{P}^{**}) = \sum a_{np}(\mathbf{u}_{np} - \mathbf{u}_{np}^{**}) - A_p\,[(p_p - p_p^{*}) - (p_{np} - p_{np}^{*})] \tag{A11}$$

$$p = p^{*} + p' \qquad \mathbf{u} = \mathbf{u}^{**} + \mathbf{u}' \tag{A12}$$

$$a_{ip}(\mathbf{u}'_p) = -A_p\,(p'_p - p'_{np}) \tag{A13}$$

$$\mathbf{u} = \mathbf{u}^{**} + \mathbf{u}'_p = \mathbf{u}^{**} - \frac{A_p\,(p'_p - p'_{np})}{a_{ip}} \tag{A14}$$

Note that, similar to the original PISO algorithm, for the sake of simplicity, the summation over the adjacent velocity points is omitted here ($\sum a_{np}(\mathbf{u}_{np} - \mathbf{u}_{np}^{**}) = \sum a_{np}(\mathbf{u}'_{np}) \approx 0$). Substituting Eq.

(A14) into the discretized continuity equation yields the first system of discrete pressure-correction equation as:

$$a_{i,j}P'_{i,j} = a_{i+1,j}P'_{i+1,j} + a_{i-1,j}P'_{i-1,j} + a_{i,j+1}P'_{i,j+1} + a_{i,j-1}P'_{i,j-1} + b_{i,j} - \frac{3\rho_p^{n+1} - 4\rho_p^{n} + \rho_p^{n-1}}{2\Delta t\rho_p^{n+1}}\Delta x\Delta y \tag{A15}$$

$$\begin{aligned} & a_{i,j} = a_{i+1,j} + a_{i-1,j} + a_{i,j+1} + a_{i,j-1} \\ & a_{i+1,j} = d_{i+1,j}\Delta y, \quad a_{i-1,j} = d_{i,j}\Delta y \\ & a_{i,j+1} = d_{i,j+1}\Delta x, \quad a_{i,j-1} = d_{i,j}\Delta x \\ & b_{i,j} = \overset{**}{u}_{i,j}\Delta y - \overset{**}{u}_{i+1,j}\Delta y + \overset{\sim **}{v}_{i,j}\Delta x - \overset{\sim **}{v}_{i,j+1}\Delta x \end{aligned} \tag{A16}$$

Once the above equation is solved, the velocity and pressure fields can be modified via Eqs. (A12) and (A14) as:

$$\begin{aligned} & p = p^{*} + \alpha_{p1}p' \\ & \mathbf{u} = \mathbf{u}^{**} - \frac{A_p\,(p'_p - p'_{np})}{a_{ip}} \end{aligned} \tag{A17}$$

where α_{p1} denotes the first under-relaxation factor which is taken as unity in the current work. Once again it is assumed that the newly corrected velocity (**u**) field obtained from Eq. (17) is still not divergence free ($\nabla \cdot \mathbf{u} \neq 0$) and therefore cannot satisfy the continuity equation rigorously. This assumption means that before advancing to the next time step (*n+1*), the second pressure-correction step as a main part of the PISO algorithm is needed to reach a satisfactory degree of consistency. Thus, similar to the previous step, the superscripts of the modified velocity and pressure fields in Eq. (A17) are replaced by $\mathbf{u} \rightarrow \mathbf{u}^{***}$ and $p \rightarrow p^{**}$. By substituting the second semi-corrected velocity ($\mathbf{u}^{***}$) and pressure (p^{**}) values into the momentum equation, the third modified velocity ($\mathbf{u}^{***}$) can be obtained as:

$$\mathbf{u}_p^{***} = \frac{\sum a_{np}\mathbf{u}_{np}^{***} + S_u + S_t}{a_{ip}} - \frac{A_p(p_p^{**} - p_{np}^{**})}{a_{ip}} \tag{A18}$$

It is important to note that, contrary to the classical PISO algorithm, due to the utilization of modified velocity and pressure values in momentum equation, the central (a_{ip}) and neighbor (a_{np}) coefficients in Eq. (A10) are replaced by the updated coefficients a_{ip} and a_{np} in Eq. (A18). Our results have shown that, this modification has a significant impact on the accuracy and convergence rate of numerical solution in dealing with the convection-dominated flows. To terminate the methodology, it is assumed that the correct pressure field (p^{n+1}) with the aid of the newly updated velocity field ($\overset{***}{\mathbf{u}}$) can accurately ensure the mass and momentum conservation at each computation grid as:

$$\mathbf{u}^{n+1} = \frac{\sum a_{np}\overset{***}{\mathbf{u}}_{np} + S_u + S_t}{a_{ip}} - \frac{A_p(p_p^{n+1} - p_{np}^{n+1})}{a_{ip}} \tag{A19}$$

By subtracting Eq. (A19) from (A18) and defining the second incremental pressure variable (p''), the following relationships may be derived:

$$\mathbf{u}^{n+1} - \mathbf{u}_p^{***} = \frac{\sum a_{np}\overset{***}{\mathbf{u}}_{np} + S_u + S_t}{a_{ip}} - \frac{\sum a_{np}\mathbf{u}_{np}^{***} + S_u + S_t}{a_{ip}} - \frac{A_p(p_p^{n+1} - p_{np}^{n+1})}{a_{ip}} + \frac{A_p(p_p^{**} - p_{np}^{**})}{a_{ip}} \tag{A20}$$

$$p^{n+1} = p^{**} + \alpha_{p2}p'' \tag{A21}$$

$$\mathbf{u}^{n+1} = \mathbf{u}_p^{***} + \frac{\sum a_{np}(\overset{***}{\mathbf{u}}_{np} - \mathbf{u}_{np}^{***})}{a_{ip}} - \frac{A_p(p''_p - p''_{np})}{a_{ip}} \tag{A22}$$

where $\alpha_{p2} = 1$ is the second under-relaxation factor. Substitution of $\mathbf{u}^{n+1}$ in the discretized continuity equation results in the second partial differential equation for the incremental pressure given by:

$$a_{i,j}P''_{i,j} = a_{i+1,j}P''_{i+1,j} + a_{i-1,j}P''_{i-1,j} + a_{i,j+1}P''_{i,j+1} + a_{i,j-1}P''_{i,j-1} + \tilde{b}_{i,j} + \tilde{\tilde{b}}_{i,j} - \frac{3\rho_p^{n+1} - 4\rho_p^{n} + \rho_p^{n-1}}{2\Delta t\rho_p^{n+1}}\Delta x\Delta y \tag{A23}$$

$$
\begin{aligned}
&a_{i,j}=a_{i+1,j}+a_{i-1,j}+a_{i,j+1}+a_{i,j-1}\\
&a_{i+1,j}=d_{i+1,j}\Delta y,\quad a_{i-1,j}=d_{i,j}\Delta y\\
&a_{i,j+1}=d_{i,j+1}\Delta x,\quad a_{i,j-1}=d_{i,j}\Delta x\\
&\tilde{b}_{i,j}=\overset{***}{u}_{i,j}\Delta y-\overset{***}{u}_{i+1,j}\Delta y+\overset{***}{\tilde{v}}_{i,j}\Delta x-\overset{***}{\tilde{v}}_{i,j+1}\Delta x\\
&\tilde{\tilde{b}}_{i,j}=\Big(\frac{\sum a_{np}(\overset{***}{u}_{np}-u_{np}^{***})}{a_{ip}}\Big)_{i,j}\Delta y-\Big(\frac{\sum a_{np}(\overset{***}{u}_{np}-u_{np}^{***})}{a_{ip}}\Big)_{i+1,j}\Delta y\\
&+\Big(\frac{\sum \widetilde{a_{np}}(\overset{***}{\tilde{v}}_{np}-v_{np}^{***})}{\widetilde{a_{ip}}}\Big)_{i,j}\Delta x-\Big(\frac{\sum \widetilde{a_{np}}(\overset{***}{\tilde{v}}_{np}-v_{np}^{***})}{\widetilde{a_{ip}}}\Big)_{i,j+1}\Delta x
\end{aligned}
\tag{A24}
$$

Once the second pressure correction equation is solved, the exact velocity and pressure values can be computed via Eqs. (A21) and (A22). Having determined the correct velocity field, the volume fraction equation is solved and calculation is then transferred to the next time step where the updated physical quantities will be utilized as an initial guess values for the next level. However, before ending this discussion, it is worthwhile mentioning that, in the standard PISO-algorithm, Issa [56] ideally assumed that the twice-improved velocity field ($\overset{***}{\mathbf{u}}$) emerged as a source term ($\tilde{b}_{i,j}$) on the right hand side of Eq. (A24) is sufficiently accurate to fulfill zero-divergence constraint ($\nabla\cdot\overset{***}{\mathbf{u}}=0, \tilde{b}_{i,j}=0$). However, our results have revealed that this assumption is not necessarily valid such that the strict enforcement of the continuity constraint via the direct imposition of $\nabla\cdot\overset{***}{\mathbf{u}}=0$ (or $\tilde{b}_{i,j}=0$) in Eq. (A24) may lead to unphysical pressure/velocity fluctuation in highly nonlinear multi-fluid flow problems.

References

[1] M.S. Alagha, P. Szentannai, Experimentally-assessed multi-phase CFD modeling of segregating gas-solid fluidized beds, Chem. Eng. Res. Des. (2021).

[2] E. Zhou, B. Lv, X. Deng, X. Qin, C. Fang, Hydrodynamic and separation performance of gas–solid separation fluidized bed with two-size-orifice distributor, Chem. Eng. Res. Des. 168 (2021) 397–410.

[3] J.P. Moris, A.B. Kennedy, J.J. Westerink, Tsunami wave run-up load reduction inside a building array, Coast. Eng. (2021) 103910.

[4] W.C. Moon, H.T. Puay, T.L. Lau, Robust and efficient 3-D numerical model for the hydrodynamic simulation of tsunami wave on land, Adv. Water Resour. 146 (2020) 103762.

[5] E. Zhao, J. Sun, Y. Tang, L. Mu, H. Jiang, Numerical investigation of tsunami wave impacts on different coastal bridge decks using immersed boundary method, Ocean Eng. 201 (2020) 107132.

[6] Q. Zhao, W. Ren, Z. Zhang, A Thermodynamically Consistent Model and Its Conservative Numerical Approximation for Moving Contact Lines with Soluble Surfactants, ArXiv Prepr. ArXiv2104.02626. (2021).

[7] H. Hao, J. Yu, Y. Song, F. Chen, T. Liu, Deformation and regimes of liquid column during water exit of a partially submerged sphere using the front-tracking lattice Boltzmann method, J. Fluids Struct. 99 (2020) 103152.

[8] C.-H. Lee, C. Xu, Z. Huang, A three-phase flow simulation of local scour caused by a submerged wall jet with a water-air interface, Adv. Water Resour. 129 (2019) 373–384.

[9] J. García-Maribona, J.L. Lara, M. Maza, I.J. Losada, An efficient RANS numerical model for cross-shore beach processes under erosive conditions, Coast. Eng. (2021) 103975.

[10] J. Mao, L. Zhao, Y. Di, X. Liu, W. Xu, A resolved CFD–DEM approach for the simulation of landslides and impulse waves, Comput. Methods Appl. Mech. Eng. 359 (2020) 112750.

[11] G. Tryggvason, R. Scardovelli, S. Zaleski, Direct numerical simulations of gas–liquid multiphase flows, Cambridge University Press, 2011.

[12] F. Gibou, D. Hyde, R. Fedkiw, Sharp interface approaches and deep learning techniques for multiphase flows, J. Comput. Phys. 380 (2019) 442–463.

[13] N. Scapin, P. Costa, L. Brandt, A volume-of-fluid method for interface-resolved simulations of phase-changing two-fluid flows, J. Comput. Phys. 407 (2020) 109251.

[14] K.K. So, X.Y. Hu, N.A. Adams, Anti-diffusion interface sharpening technique for two-phase compressible flow simulations, J. Comput. Phys. 231 (2012) 4304–4323.

[15] T.J.R. Hughes, W.K. Liu, T.K. Zimmermann, Lagrangian-Eulerian finite element formulation for incompressible viscous flows, Comput. Methods Appl. Mech. Eng. 29 (1981) 329–349.

[16] S.O. Unverdi, G. Tryggvason, A front-tracking method for viscous, incompressible, multi-fluid flows, J. Comput. Phys. 100 (1992) 25–37.

[17] D.J. Torres, J.U. Brackbill, The point-set method: front-tracking without connectivity, J. Comput. Phys. 165 (2000) 620–644.

[18] Q. Zhu, J. Yan, A mixed interface-capturing/interface-tracking formulation for thermal multi-phase flows with emphasis on metal additive manufacturing processes, Comput. Methods Appl. Mech. Eng. 383 (2021) 113910.

[19] M. Sussman, P. Smereka, S. Osher, A level set approach for computing solutions to incompressible two-phase flow, J. Comput. Phys. 114 (1994) 146–159.

[20] C.W. Hirt, B.D. Nichols, Volume of fluid (VOF) method for the dynamics of free boundaries, J. Comput. Phys. 39 (1981) 201–225. doi:10.1016/0021-9991(81)90145-5.

[21] C. Daskiran, X. Xue, F. Cui, J. Katz, M.C. Boufadel, Large eddy simulation and experiment of shear breakup in liquid-liquid jet: Formation of ligaments and droplets, Int. J. Heat Fluid Flow. 89 (2021) 108810.

[22] F. Bahmanpouri, M. Daliri, A. Khoshkonesh, M.M. Namin, M. Buccino, Bed compaction effect on dam break flow over erodible bed; experimental and numerical modeling, J. Hydrol. 594 (2021) 125645.

[23] A. Issakhov, Y. Zhandaulet, Numerical study of dam break waves on movable beds for various forms of the obstacle by VOF method, Ocean Eng. 209 (2020) 107459.

[24] A. Issakhov, A. Borsikbayeva, The impact of a multilevel protection column on the propagation of a water wave and pressure distribution during a dam break: Numerical simulation, J. Hydrol. 598 (2021) 126212.

[25] L.C. Ngo, H.G. Choi, A multi-level adaptive mesh refinement for an integrated finite element/level set formulation to simulate multiphase flows with surface tension, Comput. Math. with Appl. 79 (2020) 908–933.

[26] X. Li, M. Liu, T. Dong, D. Yao, Y. Ma, VOF-DEM simulation of single bubble behavior in gas-liquid-solid mini-fluidized bed, Chem. Eng. Res. Des. (2020).

[27] F. Gibou, R. Fedkiw, S. Osher, A review of level-set methods and some recent applications, J. Comput. Phys. 353 (2018) 82–109.

[28] X. Yin, I. Zarikos, N.K. Karadimitriou, A. Raoof, S.M. Hassanizadeh, Direct simulations of two-phase flow experiments of different geometry complexities using Volume-of-Fluid (VOF) method, Chem. Eng. Sci. 195 (2019) 820–827.

[29] T. Marić, D.B. Kothe, D. Bothe, Unstructured un-split geometrical volume-of-fluid methods–a review, J. Comput. Phys. 420 (2020) 109695.

[30] S.K. Choi, H.Y. Nam, M. Cho, A comparison of higher-order bounded convection schemes, Comput. Methods Appl. Mech. Eng. 121 (1995) 281–301.

[31] D. Zhang, C. Jiang, D. Liang, L. Cheng, A review on TVD schemes and a refined flux-limiter for steady-state calculations, J. Comput. Phys. 302 (2015) 114–154.

[32] B.B.M. Kassar, J.N.E. Carneiro, A.O. Nieckele, Curvature computation in volume-of-fluid method based on point-cloud sampling, Comput. Phys. Commun. 222 (2018) 189–208.

[33] J.E. Pilliod Jr, E.G. Puckett, Second-order accurate volume-of-fluid algorithms for tracking material interfaces, J. Comput. Phys. 199 (2004) 465–502.

[34] M. V Kraposhin, M. Banholzer, M. Pfitzner, I.K. Marchevsky, A hybrid pressure- based solver for nonideal single- phase fluid flows at all speeds, Int. J. Numer. Methods Fluids. 88 (2018) 79–99.

[35] P. Bruno, G. Di Bella, M. De Marchis, Effect of the contact tank geometry on disinfection efficiency, J. Water Process Eng. 41 (2021) 102035.

[36] J.P. Boris, D.L. Book, Flux-corrected transport. I. SHASTA, a fluid transport algorithm that works, J. Comput. Phys. 11 (1973) 38–69.

[37] A. Harten, High resolution schemes for hyperbolic conservation laws, J. Comput. Phys. 135 (1997) 260–278.

[38] B.P. Leonard, Simple high- accuracy resolution program for convective modelling of discontinuities, Int. J. Numer. Methods Fluids. 8 (1988) 1291–1318.

[39] P.K. Sweby, High resolution schemes using flux limiters for hyperbolic conservation laws, SIAM J. Numer. Anal. 21 (1984) 995–1011.

[40] F. Kemm, A comparative study of TVD- limiters—well- known limiters and an introduction of new ones, Int. J. Numer. Methods Fluids. 67 (2011) 404–440.

[41] J. Zhu, W. Rodi, A low dispersion and bounded convection scheme, Comput. Methods Appl. Mech. Eng. 92 (1991) 87–96.

[42] P.H. Gaskell, A.K.C. Lau, Curvature- compensated convective transport: SMART, a new boundedness- preserving transport algorithm, Int. J. Numer. Methods Fluids. 8 (1988) 617–641.

[43] V.G. Ferreira, R.A.B. De Queiroz, G.A.B. Lima, R.G. Cuenca, C.M. Oishi, J.L.F. Azevedo, S. McKee, A bounded upwinding scheme for computing convection-dominated transport problems, Comput. Fluids. 57 (2012) 208–224.

[44] J. Zhu, On the higher-order bounded discretization schemes for finite volume computations of incompressible flows, Comput. Methods Appl. Mech. Eng. 98 (1992) 345–360.

[45] H. Jasak, H.G. Weller, A.D. Gosman, High resolution NVD differencing scheme for arbitrarily unstructured meshes, Int. J. Numer. Methods Fluids. 31 (1999) 431–449.

[46] B. Van Leer, Towards the ultimate conservative difference scheme. II. Monotonicity and conservation combined in a second-order scheme, J. Comput. Phys. 14 (1974) 361–370.

[47] O. Ubbink, R.I. Issa, A method for capturing sharp fluid interfaces on arbitrary meshes, J. Comput. Phys. 153 (1999) 26–50.

[48] I. Malgarinos, N. Nikolopoulos, M. Gavaises, Coupling a local adaptive grid refinement technique with an interface sharpening scheme for the simulation of two-phase flow and

free-surface flows using VOF methodology, J. Comput. Phys. 300 (2015) 732–753.

[49] V.-T. Nguyen, W.-G. Park, A volume-of-fluid (VOF) interface-sharpening method for two-phase incompressible flows, Comput. Fluids. 152 (2017) 104–119.

[50] T. Wacławczyk, T. Koronowicz, Comparison of CICSAM and HRIC high-resolution schemes for interface capturing, J. Theor. Appl. Mech. 46 (2008) 325–345.

[51] F. Garoosi, T. Mahdi, Presenting a novel higher-order bounded convection scheme for simulation of multiphase flows and convection heat transfer, Int. J. Heat Mass Transf. 172 (2021) 121163.

[52] G. Pozzetti, B. Peters, A multiscale DEM-VOF method for the simulation of three-phase flows, Int. J. Multiph. Flow. 99 (2018) 186–204.

[53] M. Dianat, M. Skarysz, A. Garmory, A Coupled Level Set and Volume of Fluid method for automotive exterior water management applications, Int. J. Multiph. Flow. 91 (2017) 19–38.

[54] X. Zhang, J. Wang, D. Wan, An improved multi-scale two phase method for bubbly flows, Int. J. Multiph. Flow. 133 (2020) 103460.

[55] H. Wang, H. Wang, F. Gao, P. Zhou, Z.J. Zhai, Literature review on pressure–velocity decoupling algorithms applied to built-environment CFD simulation, Build. Environ. 143 (2018) 671–678.

[56] R.I. Issa, Solution of the implicitly discretised fluid flow equations by operator-splitting, J. Comput. Phys. 62 (1986) 40–65.

[57] A.J. Chorin, Numerical solution of the Navier-Stokes equations, Math. Comput. 22 (1968) 745–762.

[58] D.L. Youngs, Time-dependent multi-material flow with large fluid distortion, Numer. Methods Fluid Dyn. (1982).

[59] B.J. Parker, D.L. Youngs, Two and three dimensional Eulerian simulation of fluid flow with material interfaces, Atomic Weapons Establishment, 1992.

[60] E.G. Puckett, A.S. Almgren, J.B. Bell, D.L. Marcus, W.J. Rider, A high-order projection method for tracking fluid interfaces in variable density incompressible flows, J. Comput. Phys. 130 (1997) 269–282.

[61] G.Y. Soh, G.H. Yeoh, V. Timchenko, An algorithm to calculate interfacial area for multiphase mass transfer through the volume-of-fluid method, Int. J. Heat Mass Transf. 100 (2016) 573–581.

[62] J.U. Brackbill, D.B. Kothe, C. Zemach, A continuum method for modeling surface tension, J. Comput. Phys. 100 (1992) 335–354.

[63] J.A. Heyns, A.G. Malan, T.M. Harms, O.F. Oxtoby, Development of a compressive surface capturing formulation for modelling free- surface flow by using the volume- of-

fluid approach, Int. J. Numer. Methods Fluids. 71 (2013) 788–804.

[64] P. Cifani, W.R. Michalek, G.J.M. Priems, J.G.M. Kuerten, C.W.M. van der Geld, B.J. Geurts, A comparison between the surface compression method and an interface reconstruction method for the VOF approach, Comput. Fluids. 136 (2016) 421–435.

[65] C.P. Zanutto, E.E. Paladino, F. Evrard, B. van Wachem, F. Denner, Modeling of interfacial mass transfer based on a single-field formulation and an algebraic VOF method considering non-isothermal systems and large volume changes, Chem. Eng. Sci. 247 (2022) 116855.

[66] M. Akhlaghi, V. Mohammadi, N.M. Nouri, M. Taherkhani, M. Karimi, Multi-Fluid VoF model assessment to simulate the horizontal air–water intermittent flow, Chem. Eng. Res. Des. 152 (2019) 48–59.

[67] H. Liu, W. Zhang, M. Jia, Y. He, An improved method for coupling the in-nozzle cavitation with Multi-fluid-quasi-VOF model for diesel spray, Comput. Fluids. 177 (2018) 20–32.

[68] Z. Peng, L. Ge, R. Moreno-Atanasio, G. Evans, B. Moghtaderi, E. Doroodchi, VOF-DEM Study of Solid Distribution Characteristics in Slurry Taylor Flow-Based Multiphase Microreactors, Chem. Eng. J. 396 (2020) 124738.

[69] R.F.L. Cerqueira, E.E. Paladino, F. Evrard, F. Denner, B. van Wachem, Multiscale modeling and validation of the flow around Taylor bubbles surrounded with small dispersed bubbles using a coupled VOF-DBM approach, Int. J. Multiph. Flow. 141 (2021) 103673.

[70] F. Abbas, B. Wang, M.J. Cleary, A.R. Masri, Numerical convergence of volume of fluid based large eddy simulations of atomizing sprays, Phys. Fluids. 33 (2021) 42119.

[71] H.K. Versteeg, W. Malalasekera, An introduction to computational fluid dynamics: the finite volume method, Pearson Education, 2007.

[72] S.-W. Kim, T.J. Benson, Comparison of the SMAC, PISO and iterative time-advancing schemes for unsteady flows, Comput. Fluids. 21 (1992) 435–454.

[73] A. Colagrossi, M. Landrini, Numerical simulation of interfacial flows by smoothed particle hydrodynamics, J. Comput. Phys. 191 (2003) 448–475.

[74] L. Lobovský, E. Botia-Vera, F. Castellana, J. Mas-Soler, A. Souto-Iglesias, Experimental investigation of dynamic pressure loads during dam break, J. Fluids Struct. 48 (2014) 407–434.

[75] Z. Sun, K. Djidjeli, J.T. Xing, Modified MPS method for the 2D fluid structure interaction problem with free surface, Comput. Fluids. 122 (2015) 47–65.

[76] I.M. Jánosi, D. Jan, K.G. Szabó, T. Tél, Turbulent drag reduction in dam-break flows, Exp. Fluids. 37 (2004) 219–229.

[77] P. Jonsson, P. Jonsén, P. Andreasson, T.S. Lundström, J.G.I. Hellström, Modelling dam break evolution over a wet bed with smoothed particle hydrodynamics: A parameter study, Engineering. 7 (2015) 248.

[78] Y. Ye, T. Xu, D.Z. Zhu, Numerical analysis of dam-break waves propagating over dry and wet beds by the mesh-free method, Ocean Eng. 217 (2020) 107969.

[79] A.J. Crespo, M. Gómez-Gesteira, R.A. Dalrymple, Modeling dam break behavior over a wet bed by a SPH technique, J. Waterw. Port, Coastal, Ocean Eng. 134 (2008) 313–320.

[80] Z.H. Gu, H.L. Wen, C.H. Yu, T.W.H. Sheu, Interface-preserving level set method for simulating dam-break flows, J. Comput. Phys. 374 (2018) 249–280.

[81] A. Khoshkonesh, B. Nsom, S. Gohari, H. Banejad, A comprehensive study on dam-break flow over dry and wet beds, Ocean Eng. 188 (2019) 106279.

[82] Z. Ghadampour, M.R. Hashemi, N. Talebbeydokhti, S.P. Neill, A.H. Nikseresht, Some numerical aspects of modelling flow around hydraulic structures using incompressible SPH, Comput. Math. with Appl. 69 (2015) 1470–1483.

[83] J. Yen, C. Lin, C. Tsai, Hydraulic characteristics and discharge control of sluice gates, J. Chinese Inst. Eng. 24 (2001) 301–310.

[84] D.R. Basco, A qualitative description of wave breaking, J. Waterw. Port, Coastal, Ocean Eng. 111 (1985) 171–188.

[85] P. Liu, J. Gao, Y. Li, Experimental investigation of submerged impinging jets in a plunge pool downstream of large dams, Sci. China Ser. E Technol. Sci. 41 (1998) 357–365.

[86] F. Garoosi, A. Shakibaeinia, Numerical simulation of Rayleigh-Bénard convection and three-phase Rayleigh-Taylor instability using a modified MPS method, Eng. Anal. Bound. Elem. 123 (2021) 1–35.

[87] G. Tryggvason, Numerical simulations of the Rayleigh-Taylor instability, J. Comput. Phys. 75 (1988) 253–282.

[88] H.-J. Kull, Theory of the Rayleigh-Taylor instability, Phys. Rep. 206 (1991) 197–325.

[89] Y. Chen, P.H. Steen, Suppression of the capillary instability in the Rayleigh–Taylor slot problem, Phys. Fluids. 8 (1996) 97–102.

[90] F. Almasi, M.S. Shadloo, A. Hadjadj, M. Ozbulut, N. Tofighi, M. Yildiz, Numerical simulations of multi-phase electro-hydrodynamics flows using a simple incompressible smoothed particle hydrodynamics method, Comput. Math. with Appl. (2019).

[91] A.C.H. Kruisbrink, F.R. Pearce, T. Yue, H.P. Morvan, An SPH multi- fluid model based on quasi buoyancy for interface stabilization up to high density ratios and realistic wave speed ratios, Int. J. Numer. Methods Fluids. 87 (2018) 487–507.

[92] A. Zainali, N. Tofighi, M.S. Shadloo, M. Yildiz, Numerical investigation of Newtonian and non-Newtonian multiphase flows using ISPH method, Comput. Methods Appl. Mech.

Eng. 254 (2013) 99–113.

[93] M. Pang, M. Lu, Numerical study on dynamics of single bubble rising in shear-thinning power-law fluid in different gravity environment, Vacuum. 153 (2018) 101–111.

[94] S.-R. Hysing, S. Turek, D. Kuzmin, N. Parolini, E. Burman, S. Ganesan, L. Tobiska, Quantitative benchmark computations of two- dimensional bubble dynamics, Int. J. Numer. Methods Fluids. 60 (2009) 1259–1288.

[95] A. Rahmat, N. Tofighi, M. Yildiz, The combined effect of electric forces and confinement ratio on the bubble rising, Int. J. Heat Fluid Flow. 65 (2017) 352–362.

[96] D. Pan, C. Chang, The capturing of free surfaces in incompressible multi- fluid flows, Int. J. Numer. Methods Fluids. 33 (2000) 203–222.

[97] Y. Zhao, H.H. Tan, B. Zhang, A high-resolution characteristics-based implicit dual time-stepping VOF method for free surface flow simulation on unstructured grids, J. Comput. Phys. 183 (2002) 233–273.

[98] J. Hua, J. Lou, Numerical simulation of bubble rising in viscous liquid, J. Comput. Phys. 222 (2007) 769–795.

[99] Ž. Tuković, M. Perić, H. Jasak, Consistent second-order time-accurate non-iterative PISO-algorithm, Comput. Fluids. 166 (2018) 78–85.

[100] S. MacNamara, G. Strang, Operator splitting, in: Split. Methods Commun. Imaging, Sci. Eng., Springer, 2016: pp. 95–114.

[101] Z. Nasri, A.H. Laatar, J. Balti, Natural convection enhancement in an asymmetrically heated channel-chimney system, Int. J. Therm. Sci. 90 (2015) 122–134.

[102] C. Varsakelis, M. V Papalexandris, A numerical method for two-phase flows of dense granular mixtures, J. Comput. Phys. 257 (2014) 737–756.

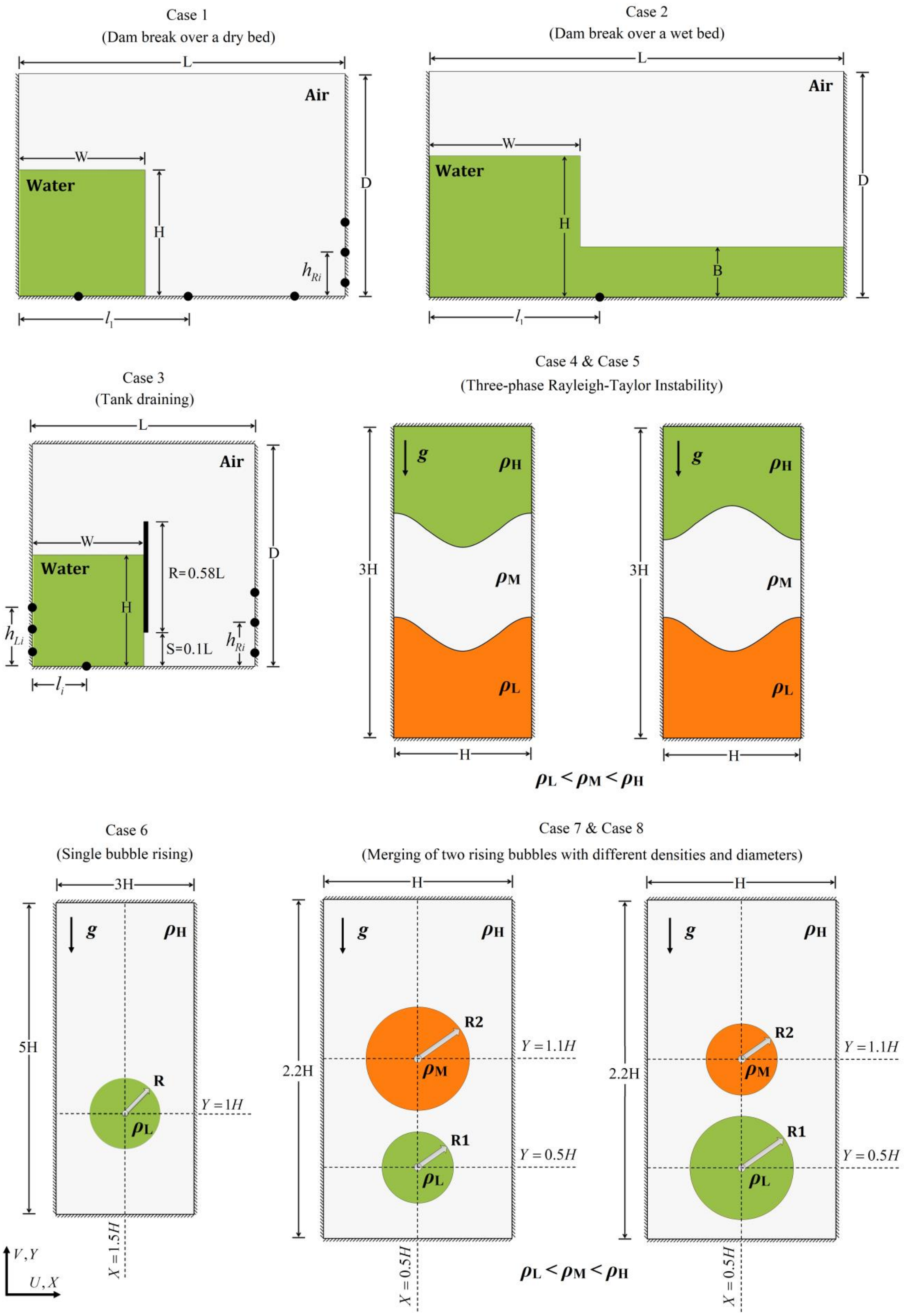

Fig. 1. Schematic diagram of eight different physical models under consideration with associated boundary conditions and coordinate system.

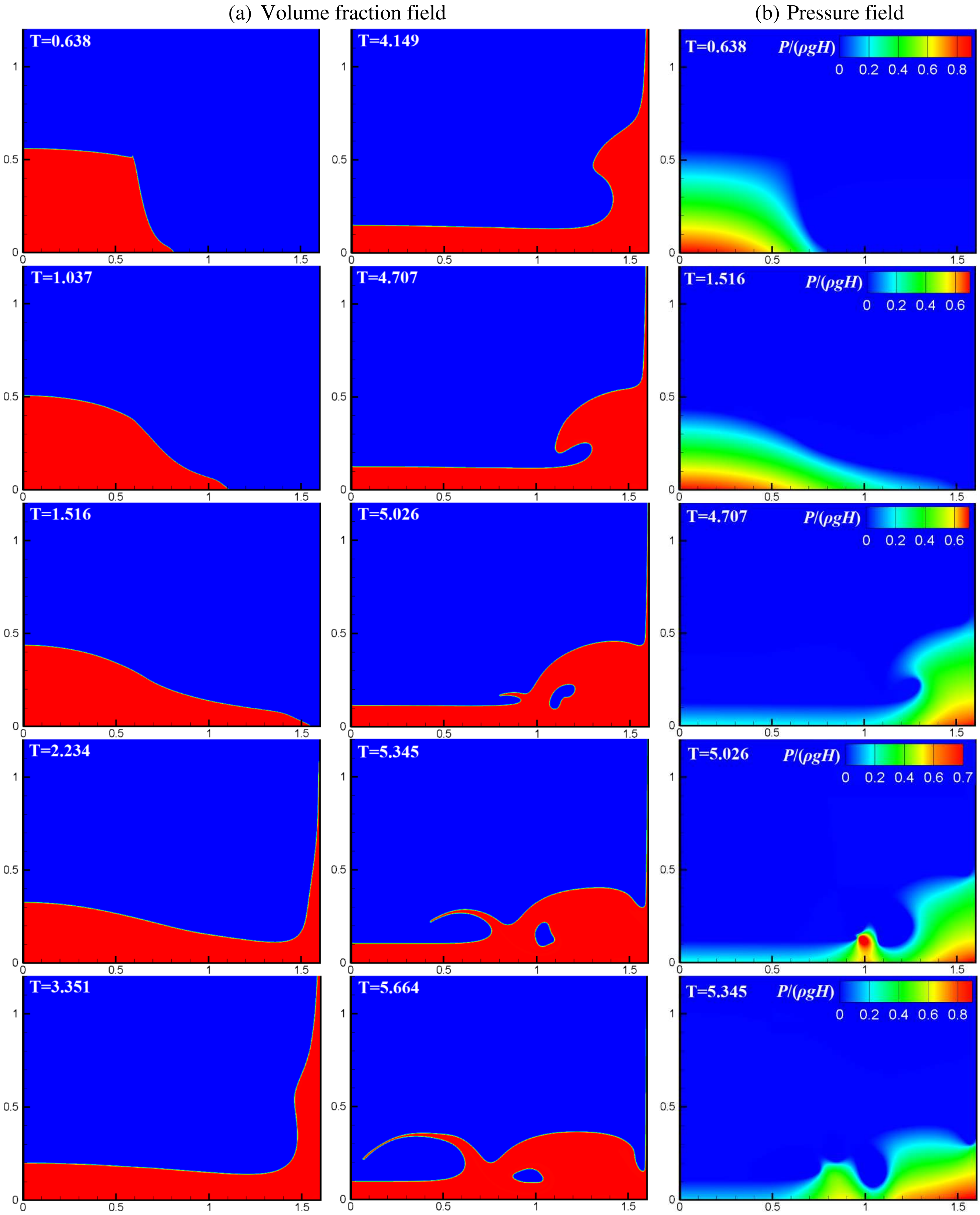
(a) Volume fraction field

(b) Pressure field

Fig. 2. Time evolution of dam-break flow over a dry bed (case 1) in terms of the volume-fraction and pressure fields calculated in the current work at different time instants.

Present work

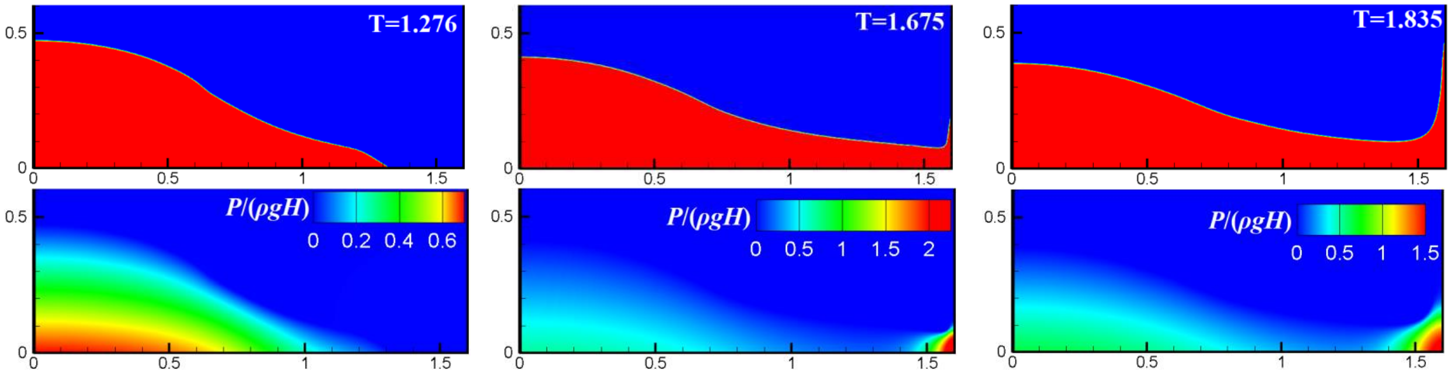

Lobovský et al. [74]

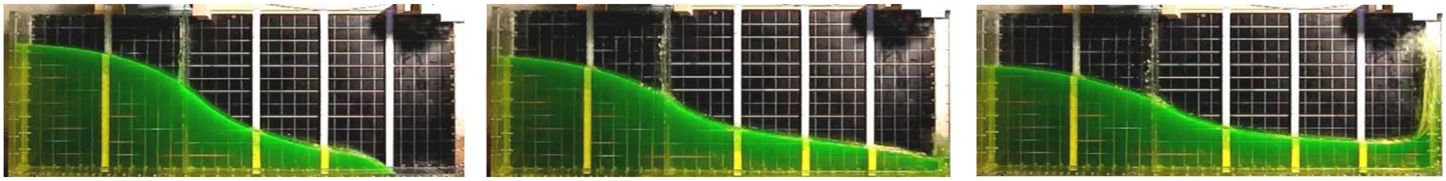

Sun et al. [75]

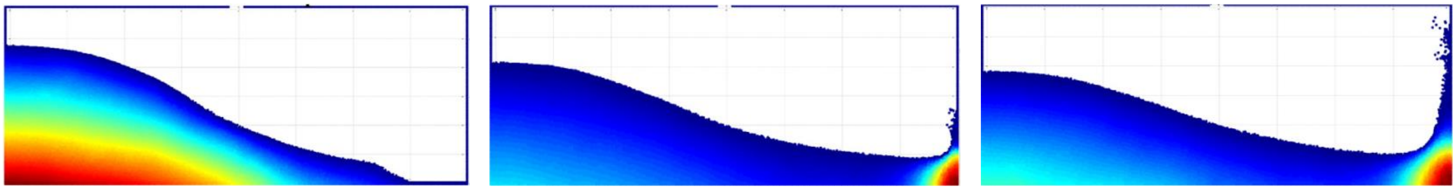

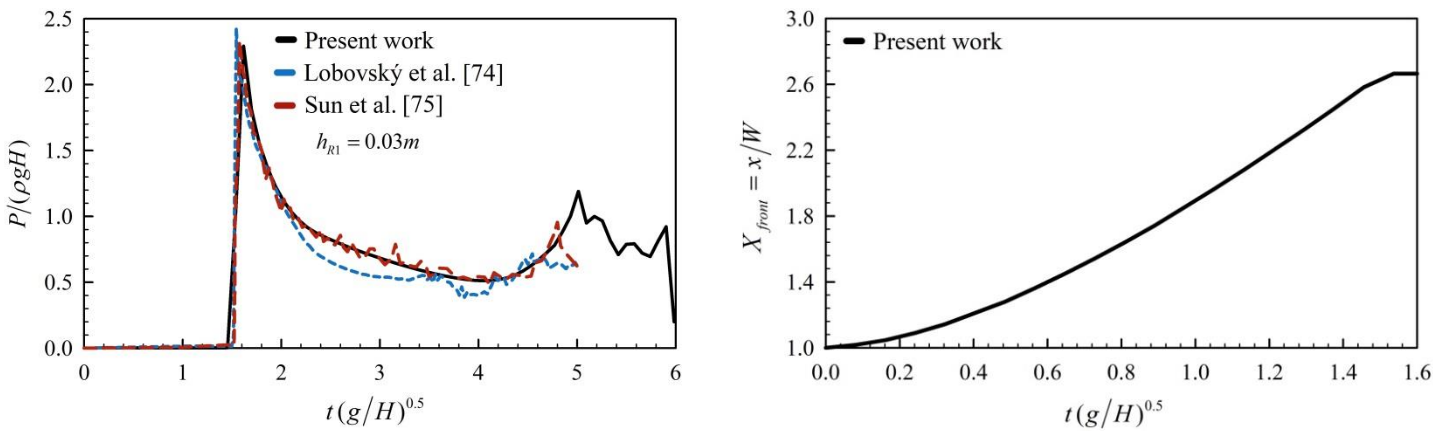

Time histories of pressure variations on the right wall

Time histories of wave front location

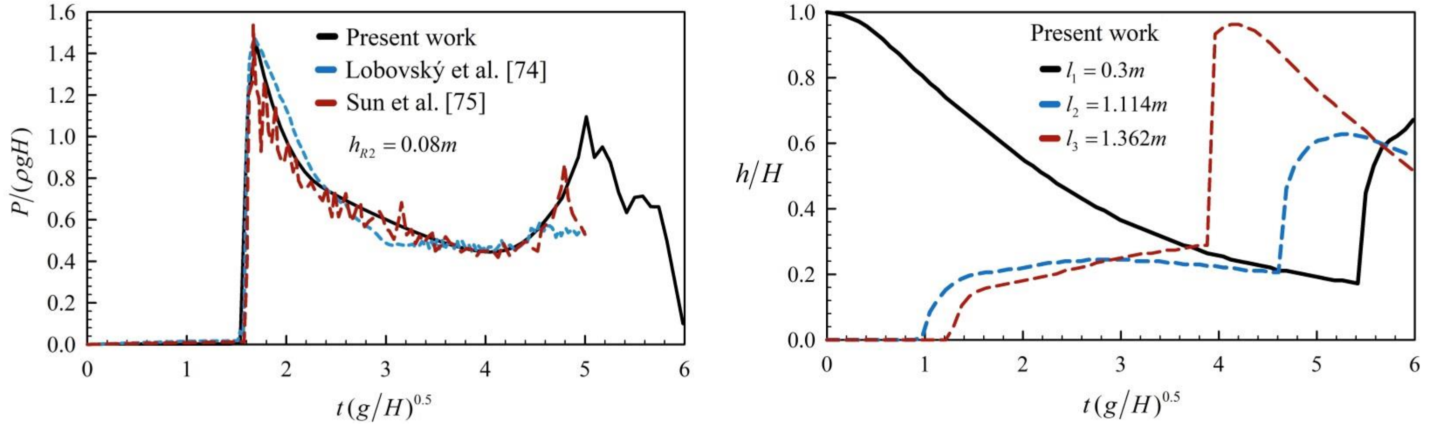

Time histories of pressure variations on the right wall

Time variation of water profile at 3 different sections

Fig. 3. Qualitative and quantitative comparison of the obtained results with numerical and experimental works of Lobovský et al. [74] and Sun et al. [75] for case 1.

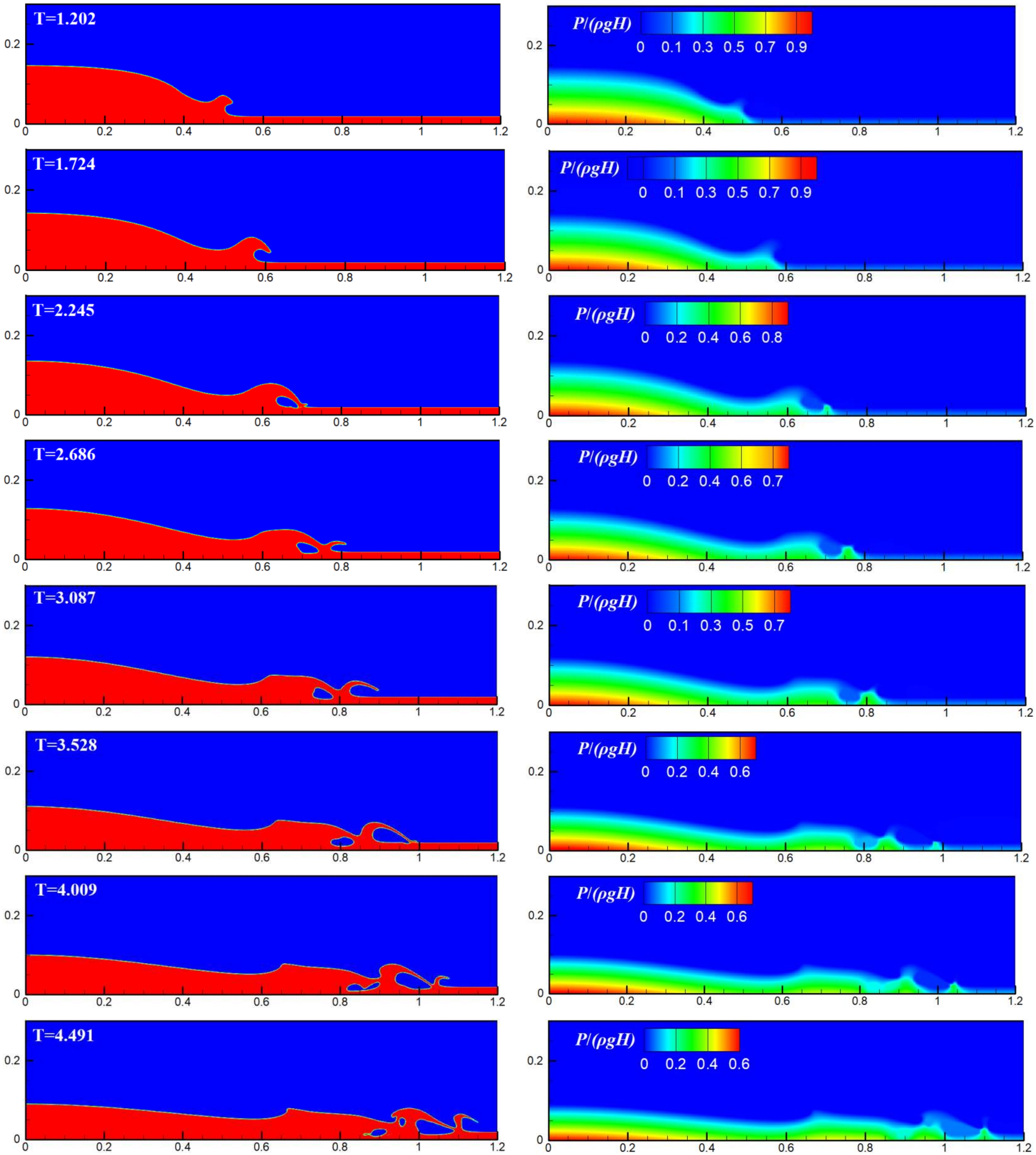

Fig. 4. Time evolution of dam-break flow over a wet bed (case 2) in terms of the volume-fraction and pressure fields calculated in the present work at different time instants.

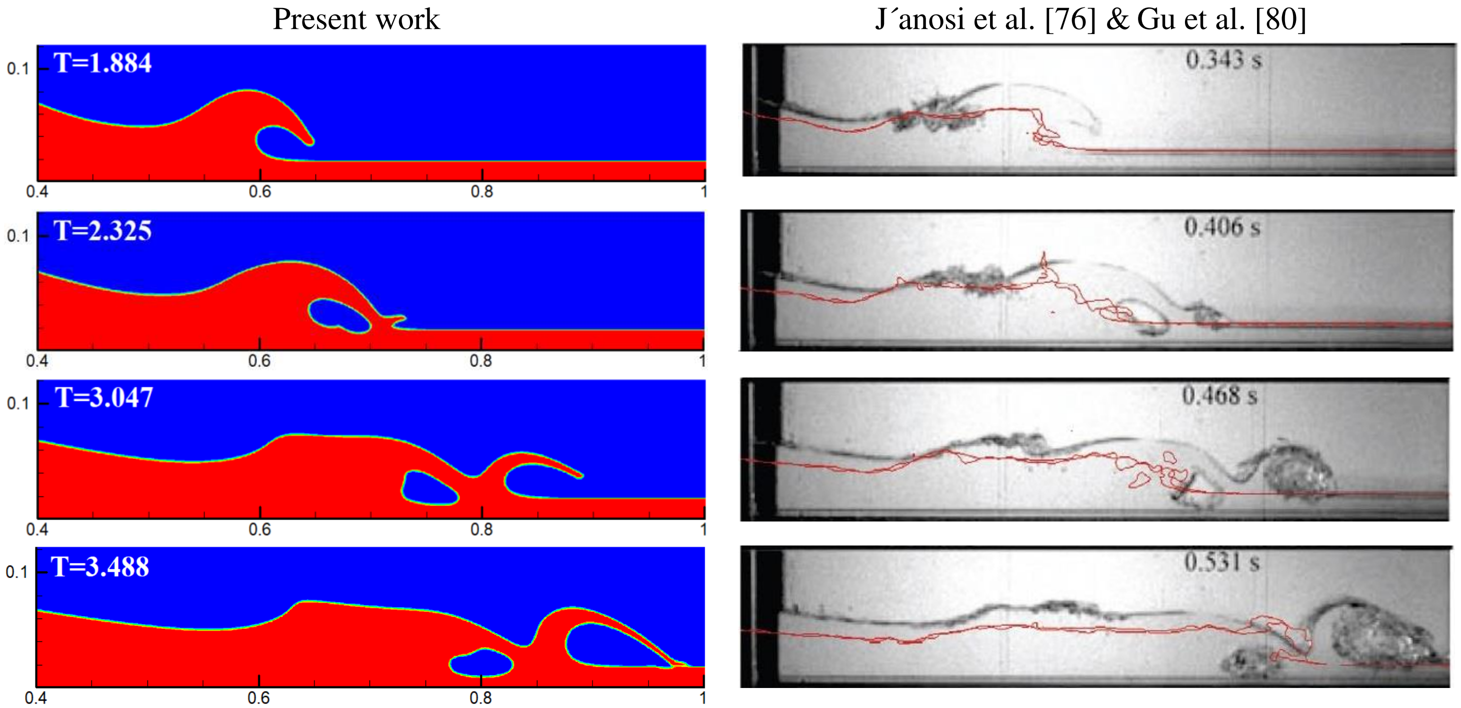

Enlarged views of the interface at three non-dimensional times

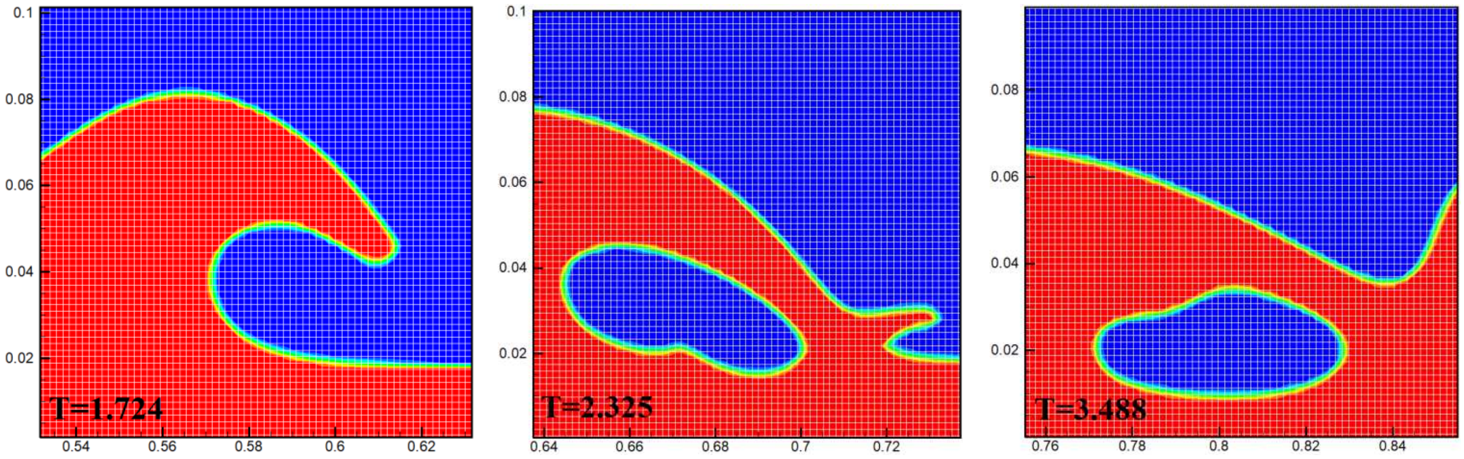

Time histories of water level depth at three different sections ($l_1 = 0.1m$, $l_2 = 0.5m$ and $l_3 = 0.9m$)

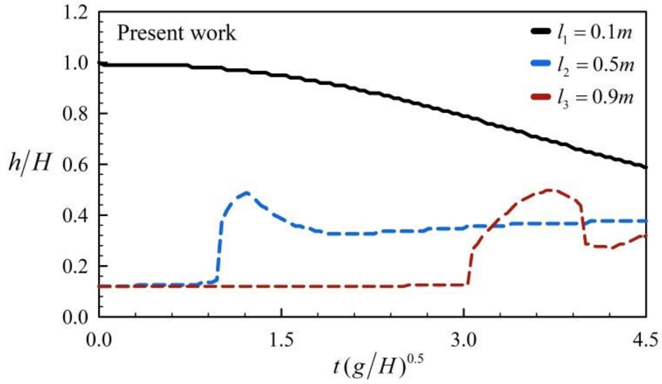

Time histories of pressure variations recorded by three different sensors installed on the bottom wall

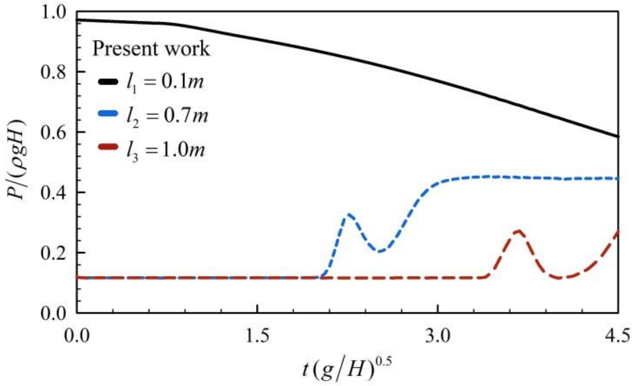

Fig. 5. Qualitative and quantitative comparison of the obtained results with numerical and experimental works of Gu et al. [80] and J´anosi et al. [76] for case 2.

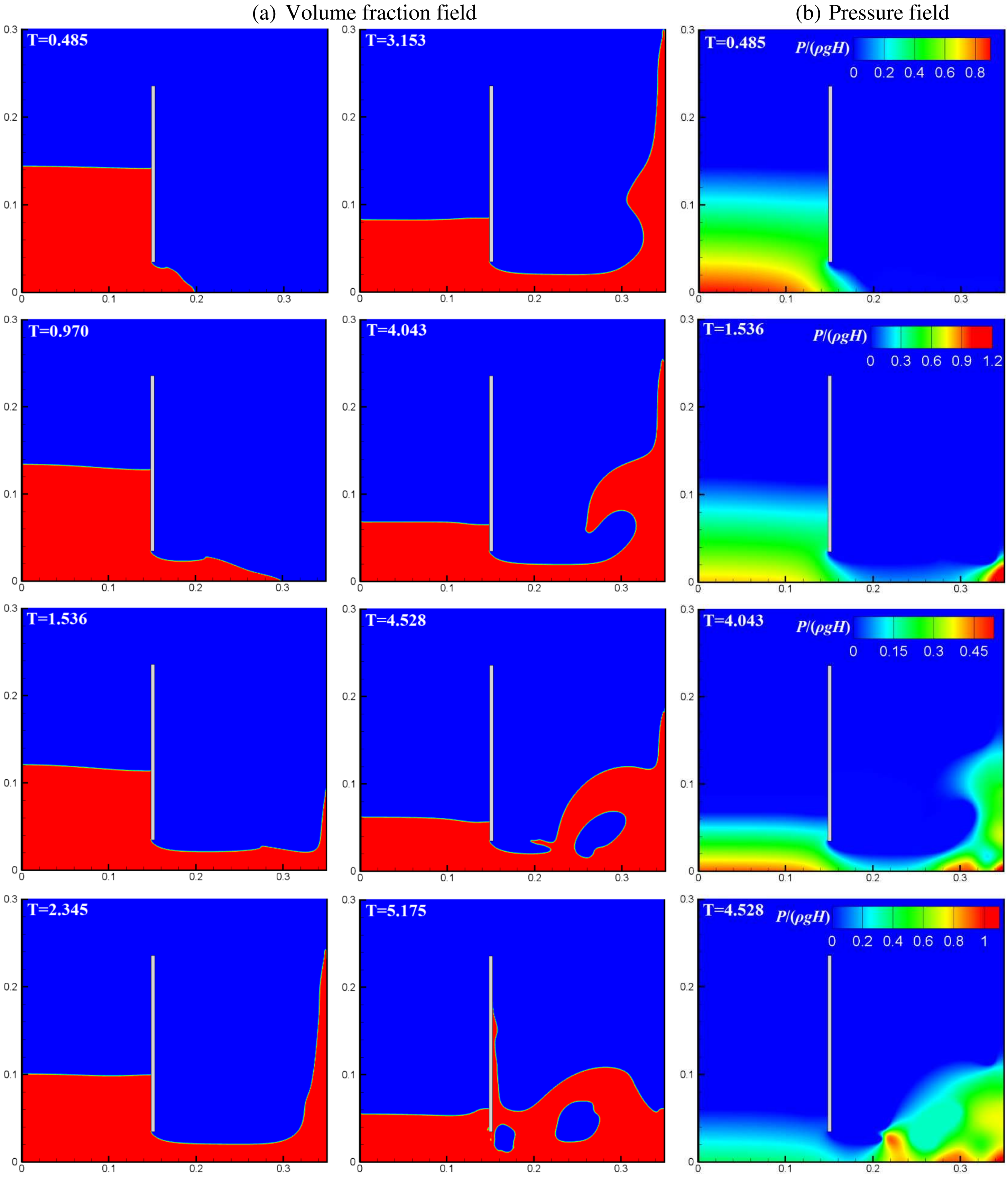
(a) Volume fraction field

(b) Pressure field

Fig. 6. Time evolution of flow under submerged gate (tank draining, case 3) calculated in the current work at different time instants.

Present work

Ghadampour et al. [82]

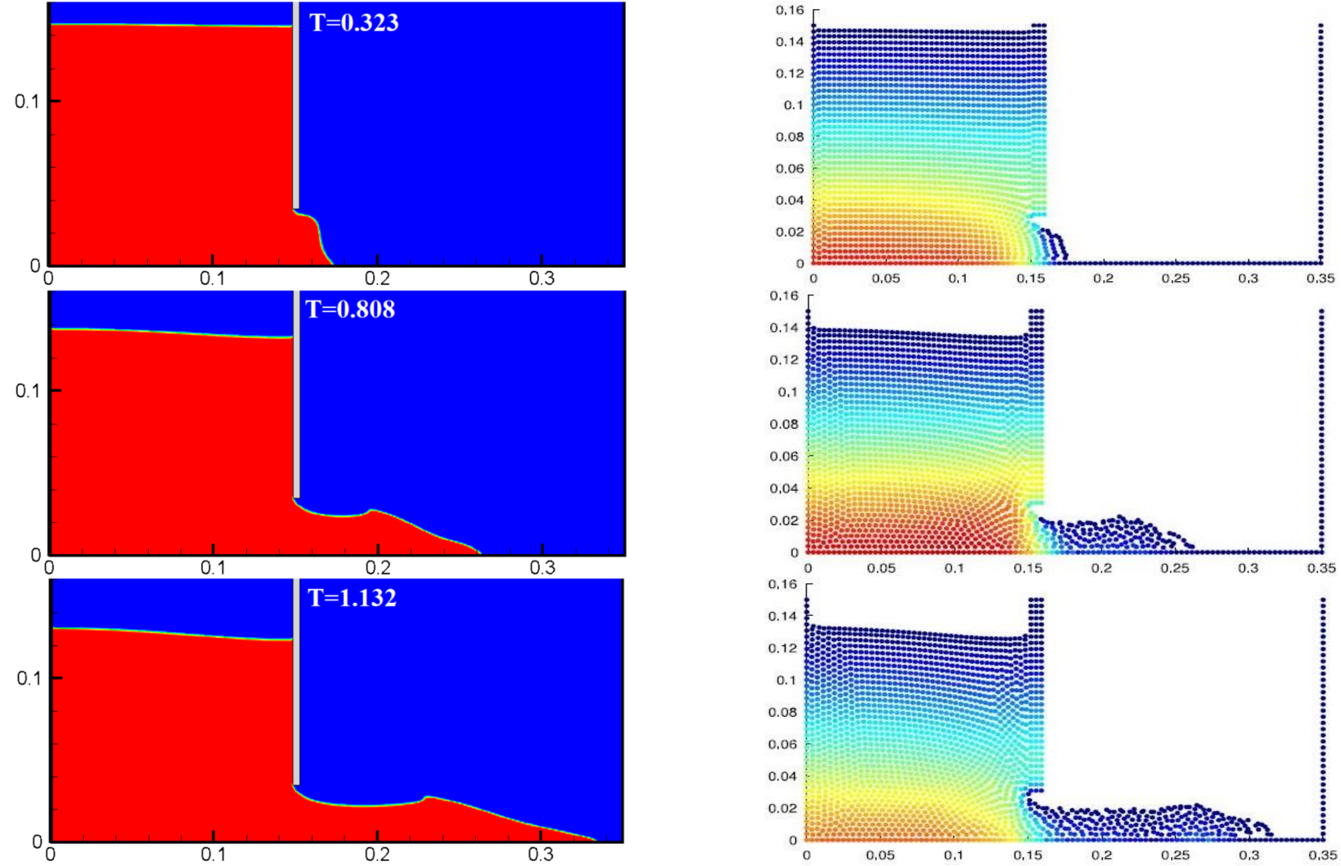

Time histories of pressure variations on the right and left walls at three different marked points

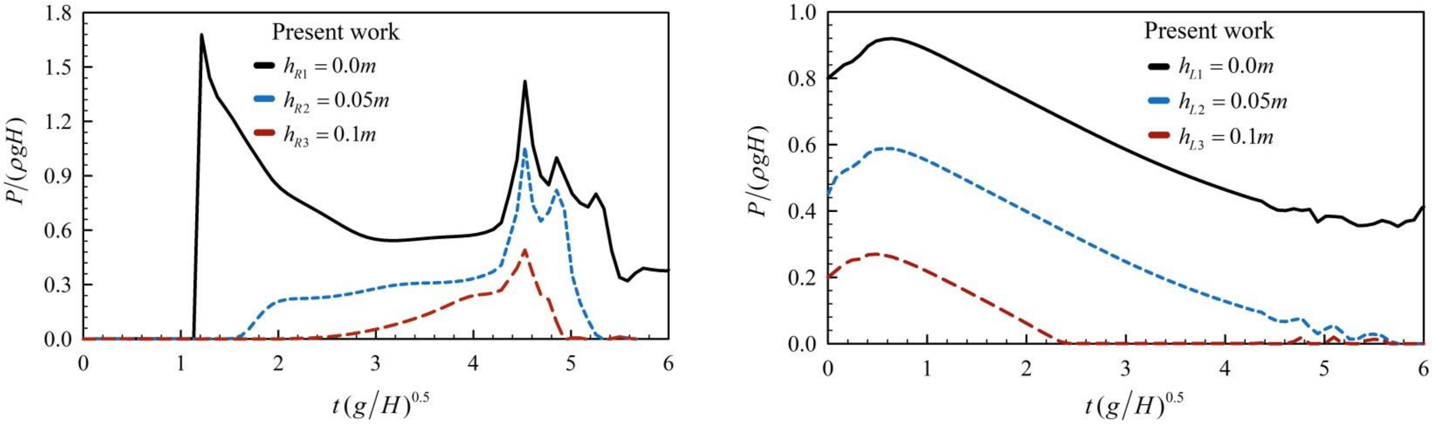

Time variation of water level height at two different sections

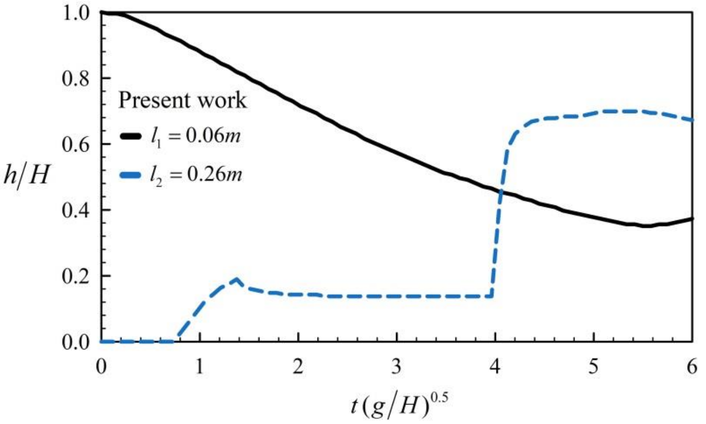

Time histories of wave front location

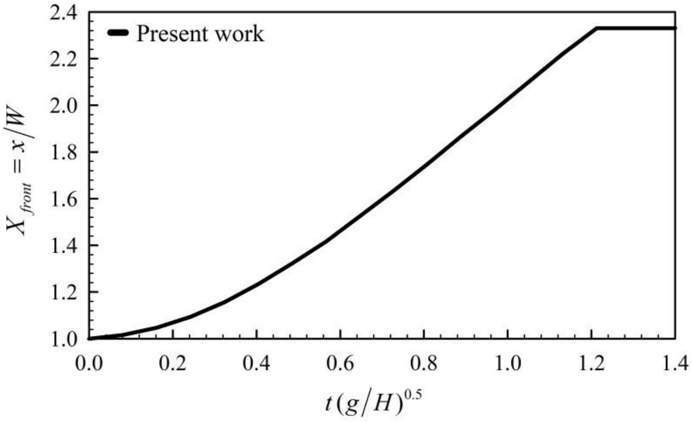

Fig. 7. Qualitative comparison of the obtained results with numerical data of Ghadampour et al. [82] in case 3.

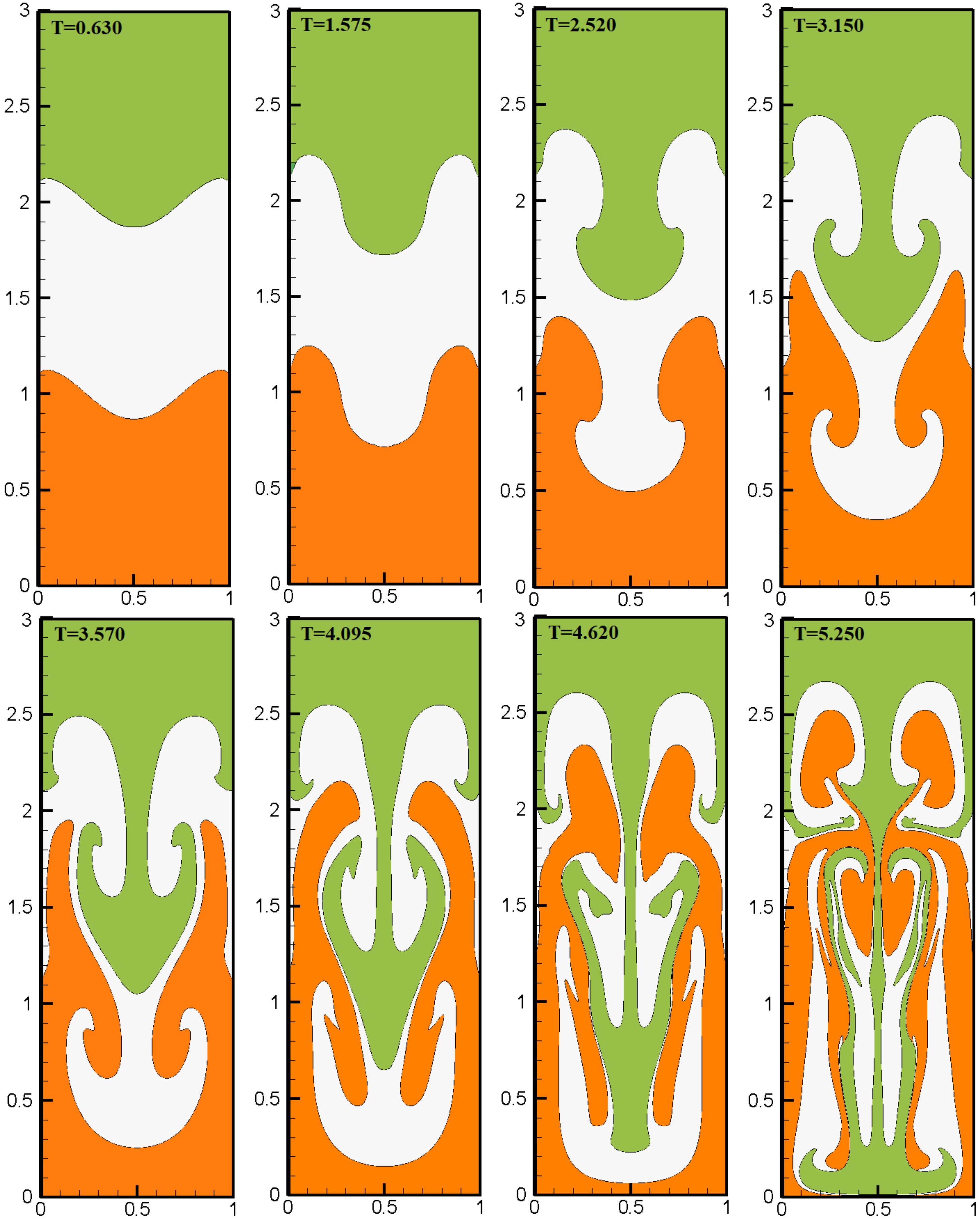

Fig. 8. Time evolution of three-phase Rayleigh-Taylor Instability (case 4) in terms of the volume-fraction field calculated in the current work at different time instants.

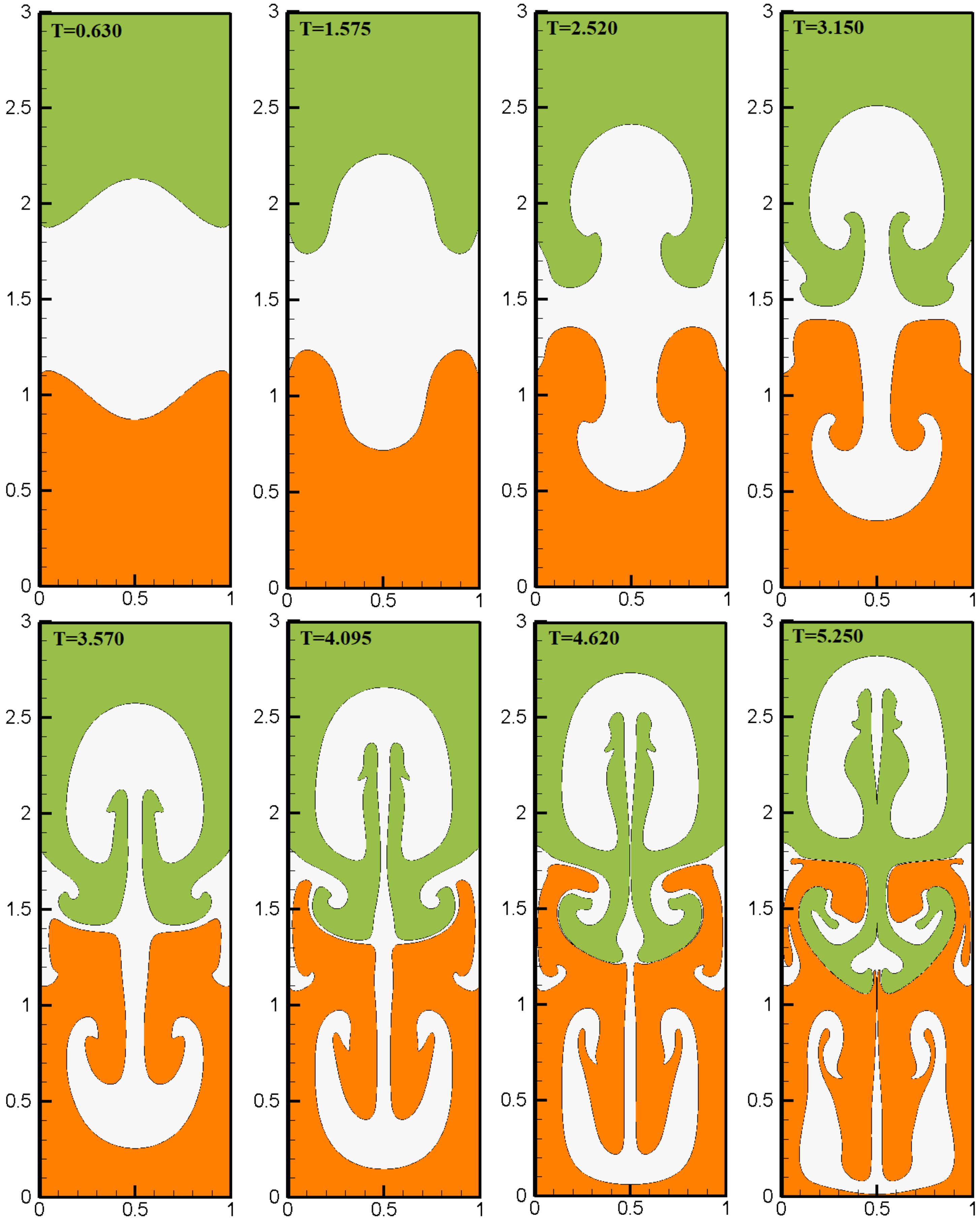

Fig. 9. Time evolution of three-phase Rayleigh-Taylor Instability (case 5) in terms of the volume-fraction field calculated in the current work at different time instants.

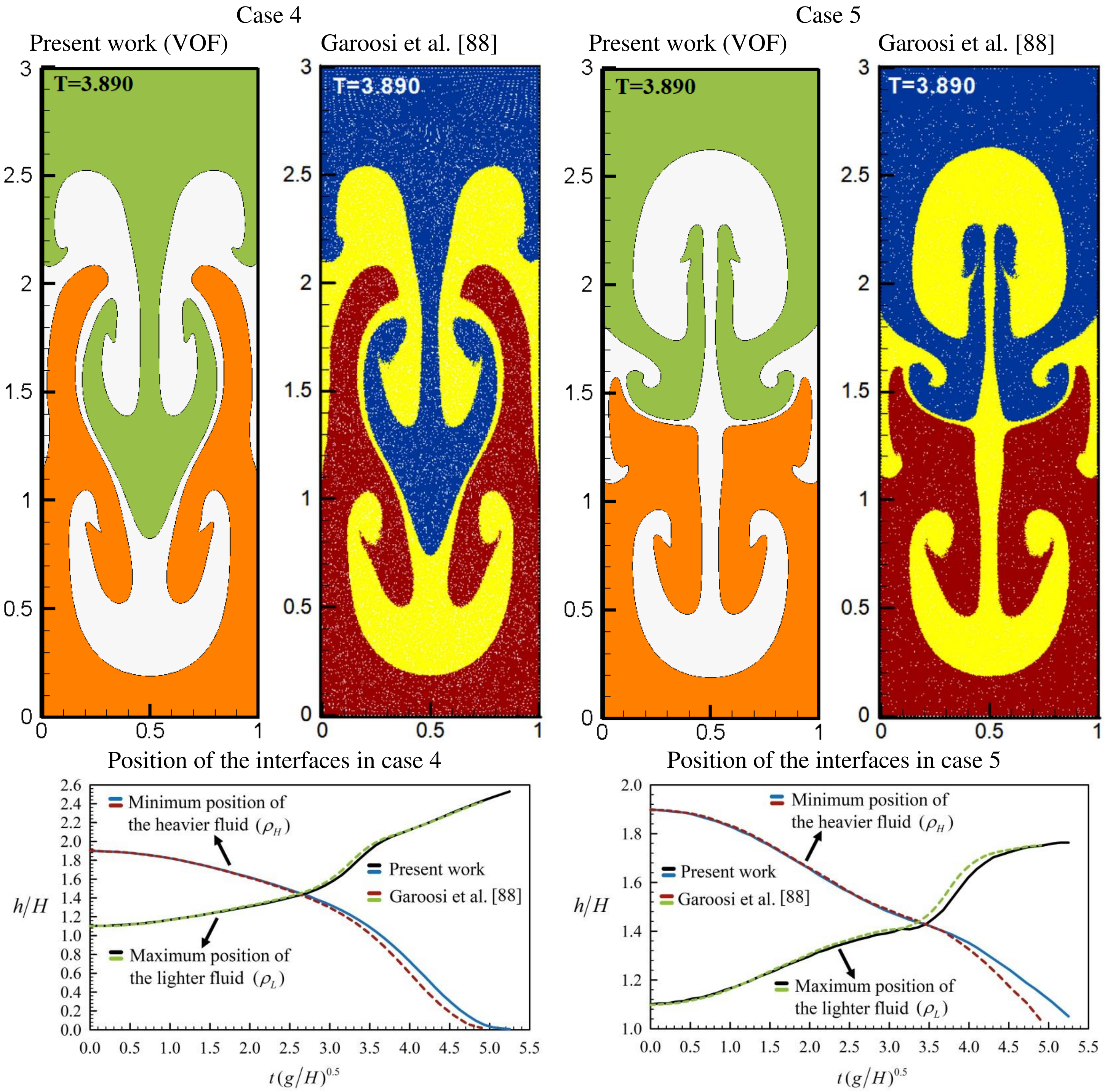
Case 4

Case 5

Present work (VOF)

Garoosi et al. [88]

Present work (VOF)

Garoosi et al. [88]

Position of the interfaces in case 4

Position of the interfaces in case 5

Fig. 10. Qualitative and quantitative comparison of the obtained results with numerical data of Garoosi et al. [88] for cases 4 and 5.

(a) Volume-fraction fields

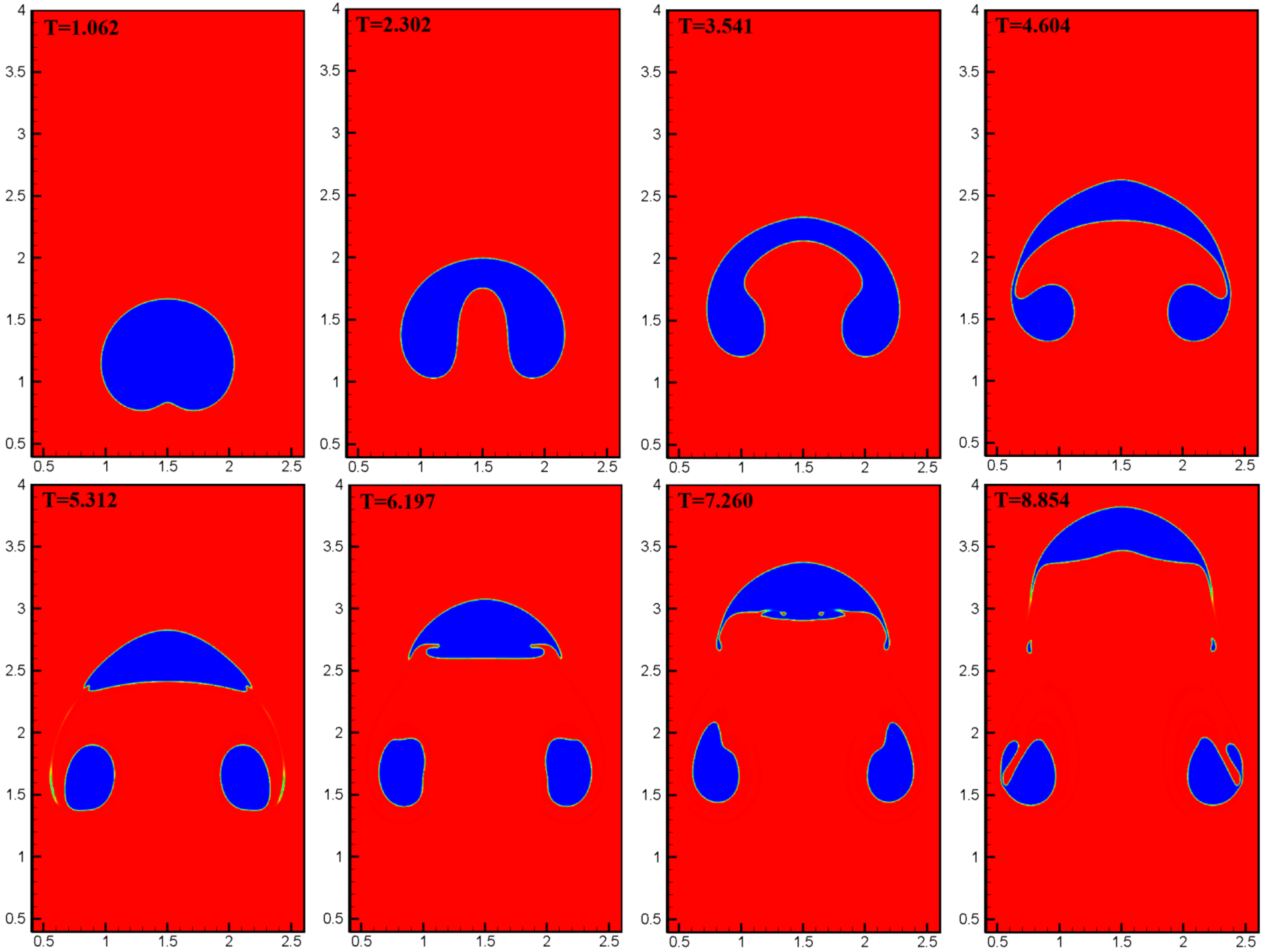

(b) Pressure fields

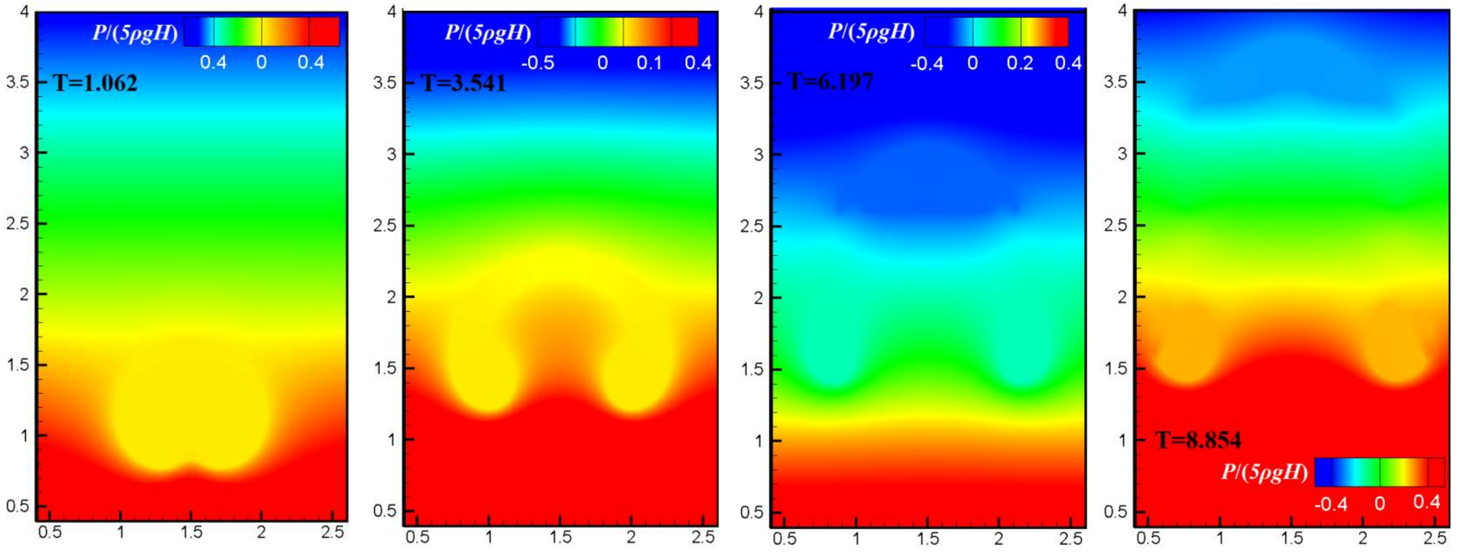

Fig. 11. Time evolution of bubble rising (case 6) in terms of the volume-fraction and pressure fields calculated in the current study at different time instants.

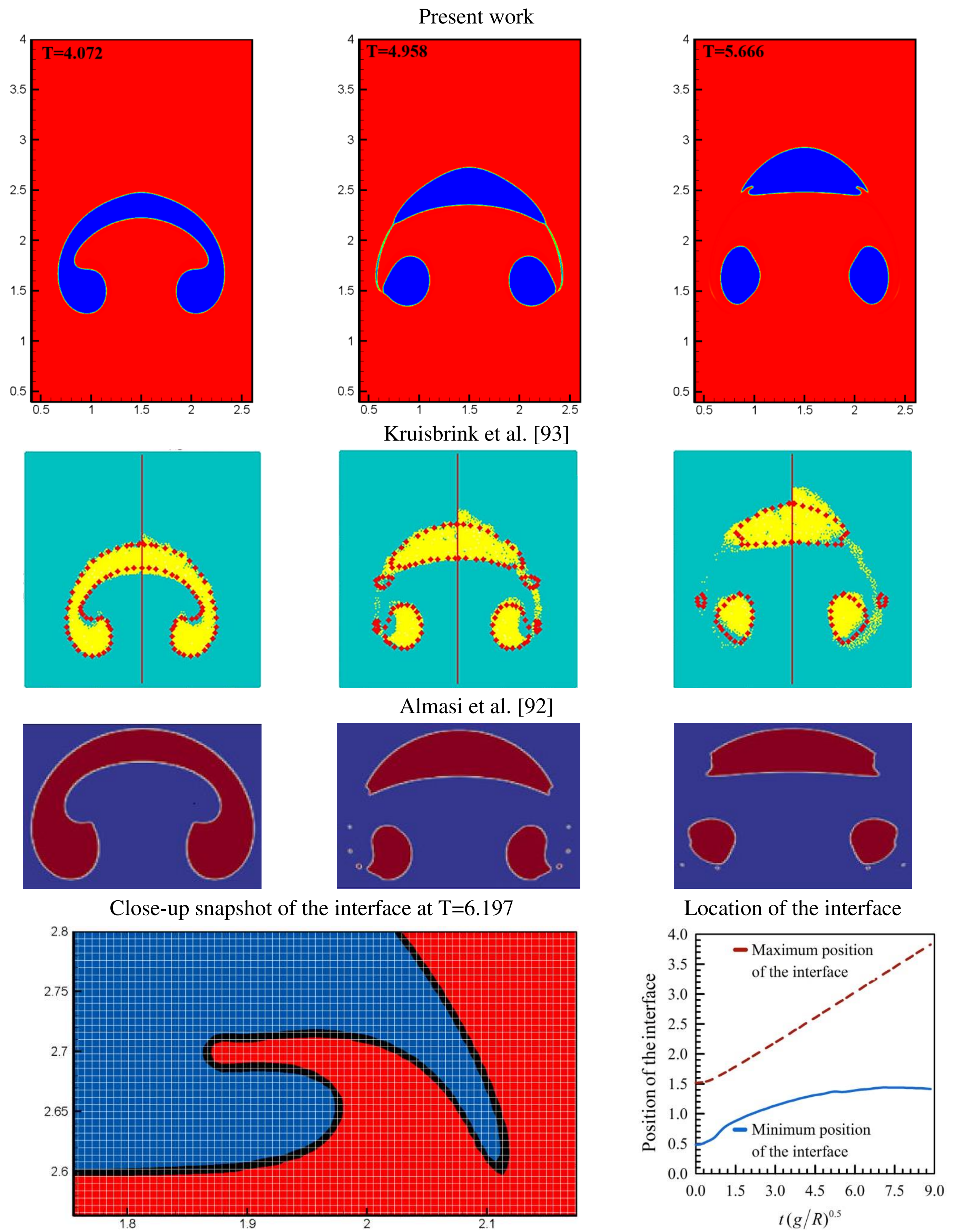

Fig. 12. Qualitative comparison of the obtained results with numerical works of Kruisbrink et al. [93] and Almasi et al. [92] for case 6 at different time instants. Zoomed-in view of the interface together with the time histories of maximum and minimum position of the bubble interface calculated in the current work.

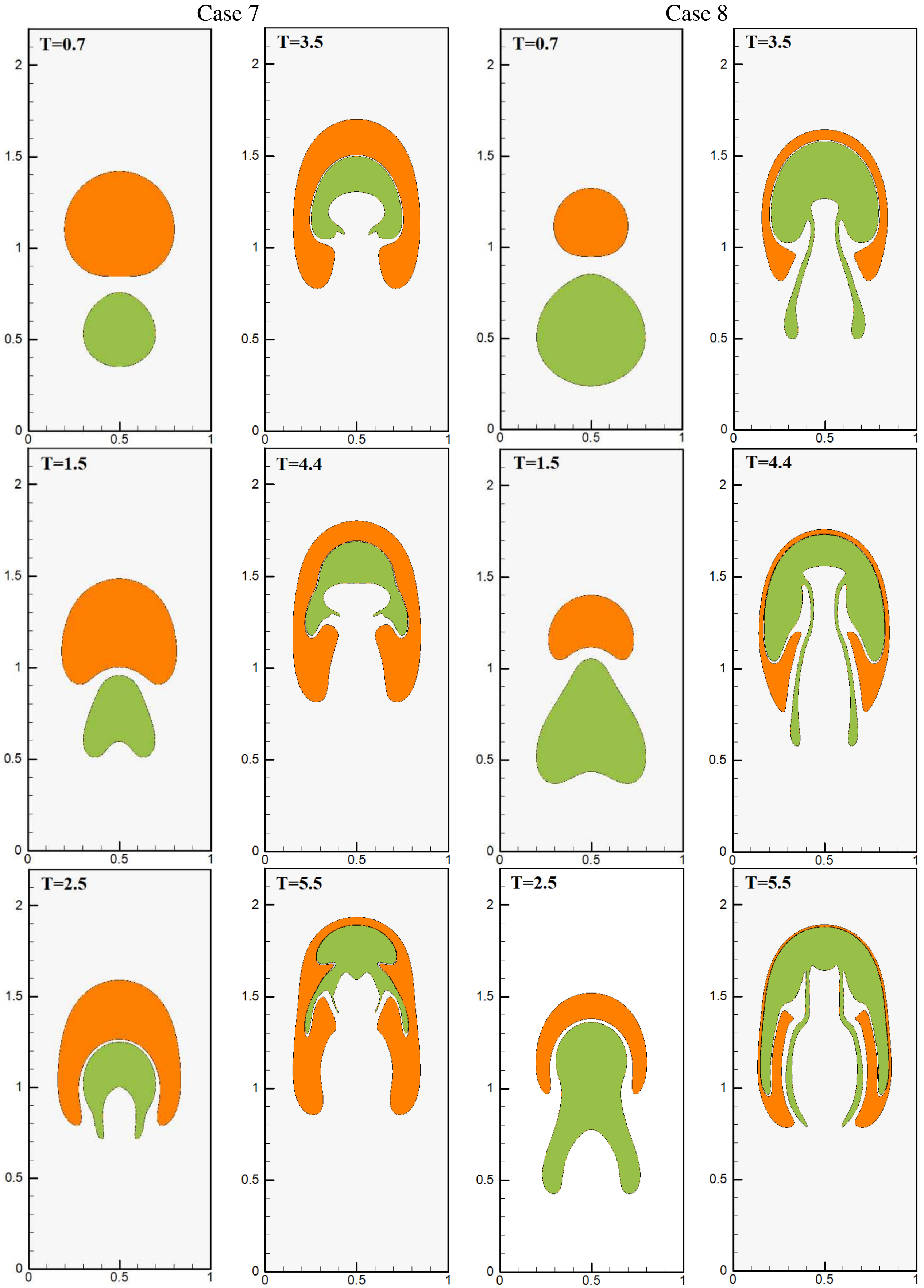

Fig. 13. Transient evolutions of merging of two rising bubbles with different densities (cases 7 & 8) in terms of the volume-fraction fields calculated in the current work at different time instants.

Case 7

Contours of non-dimensional velocity component in x-direction ($u/\sqrt{g2R_2}$)

Contours of non-dimensional velocity component in y-direction ($v/\sqrt{g2R_2}$)

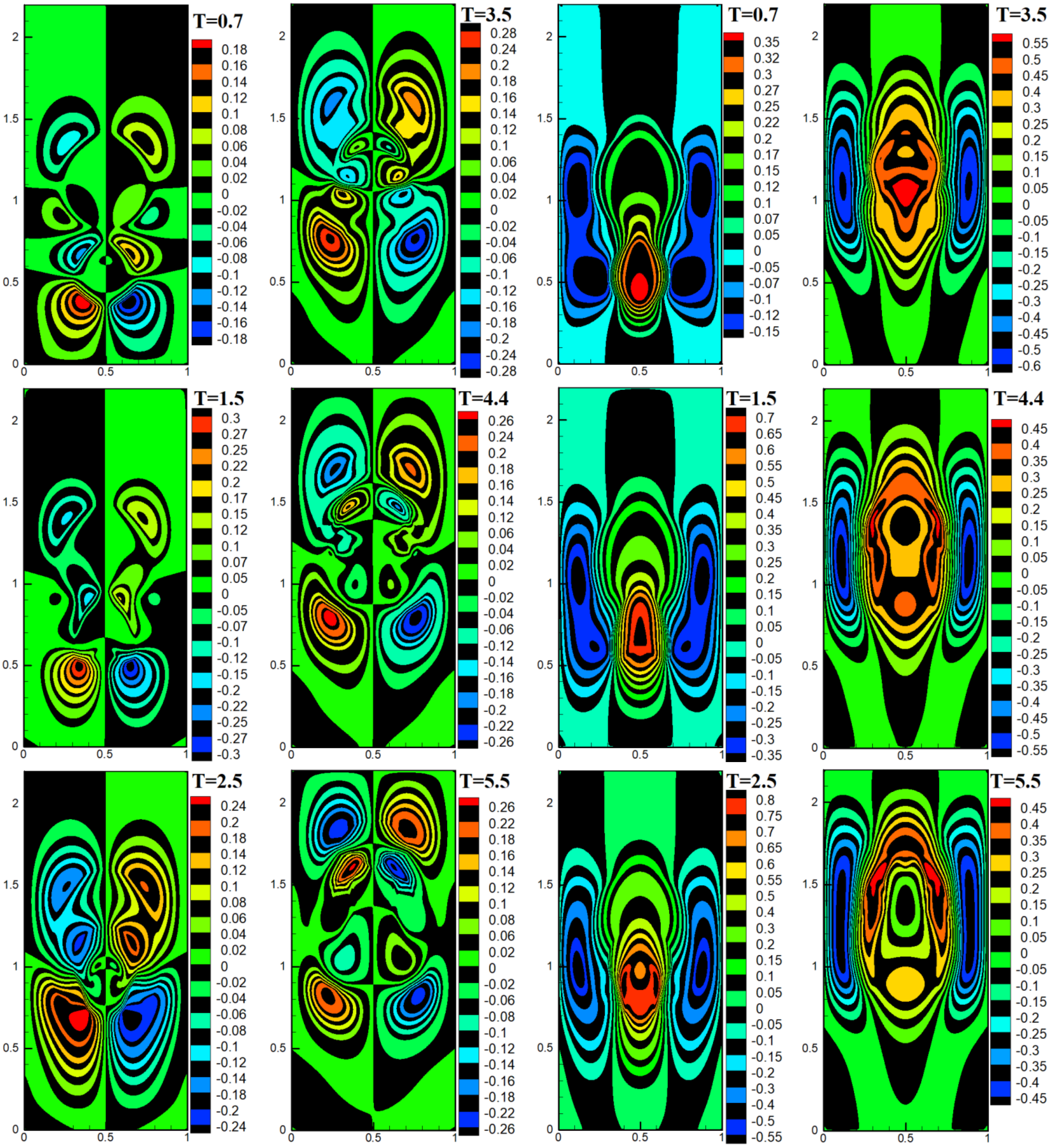

Fig. 14. Contours of non-dimensional velocity in the x and y-directions (u,v) in case 7 at different time instants.

Case 8

Contours of non-dimensional velocity component in *x*-direction ($u/\sqrt{g2R_1}$)

Contours of non-dimensional velocity component in y-direction ($v/\sqrt{g2R_1}$)

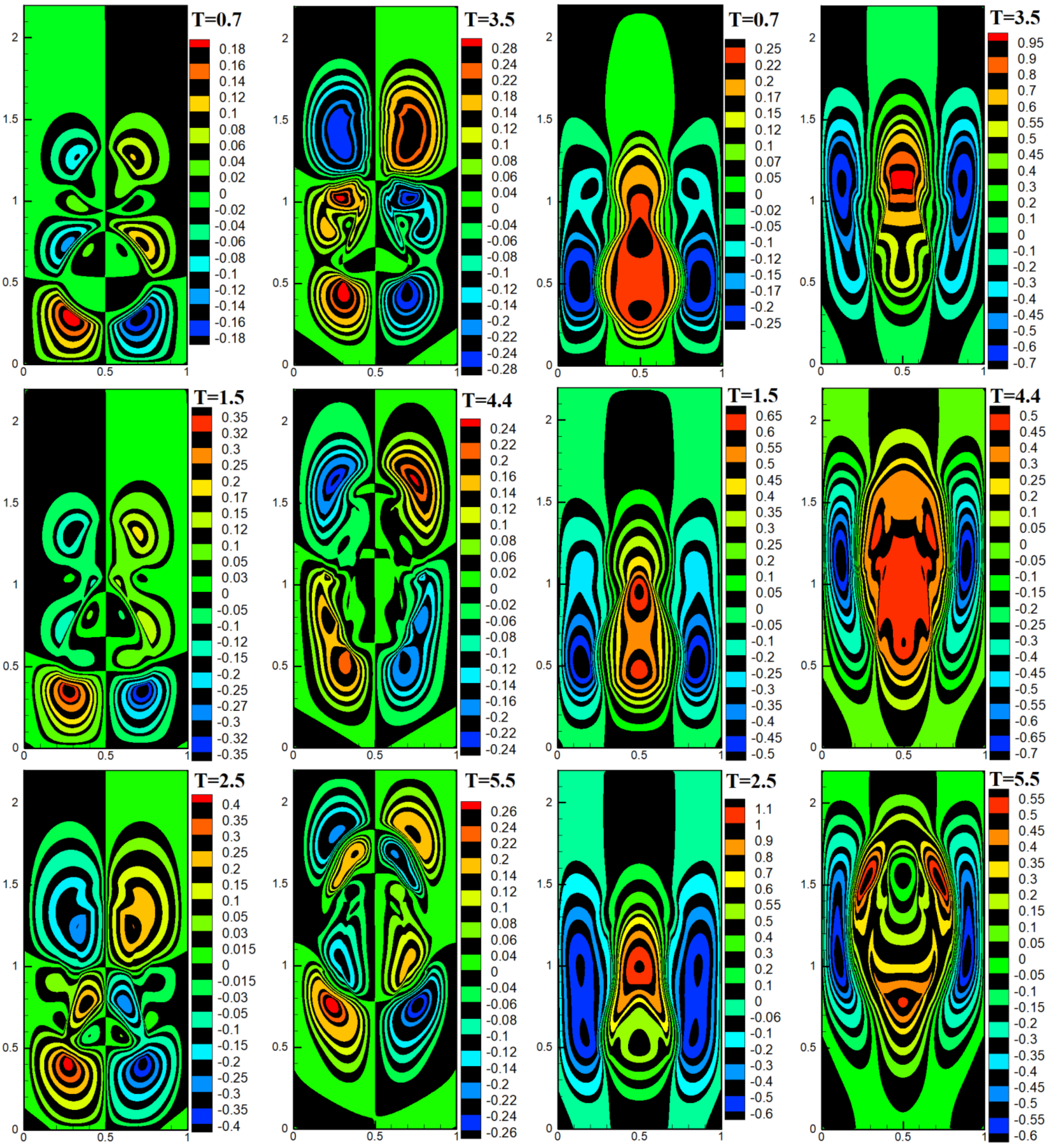

Fig. 15. Contours of non-dimensional velocity in the x and y-directions (*u*,*v*) in case 8 at different time instants.

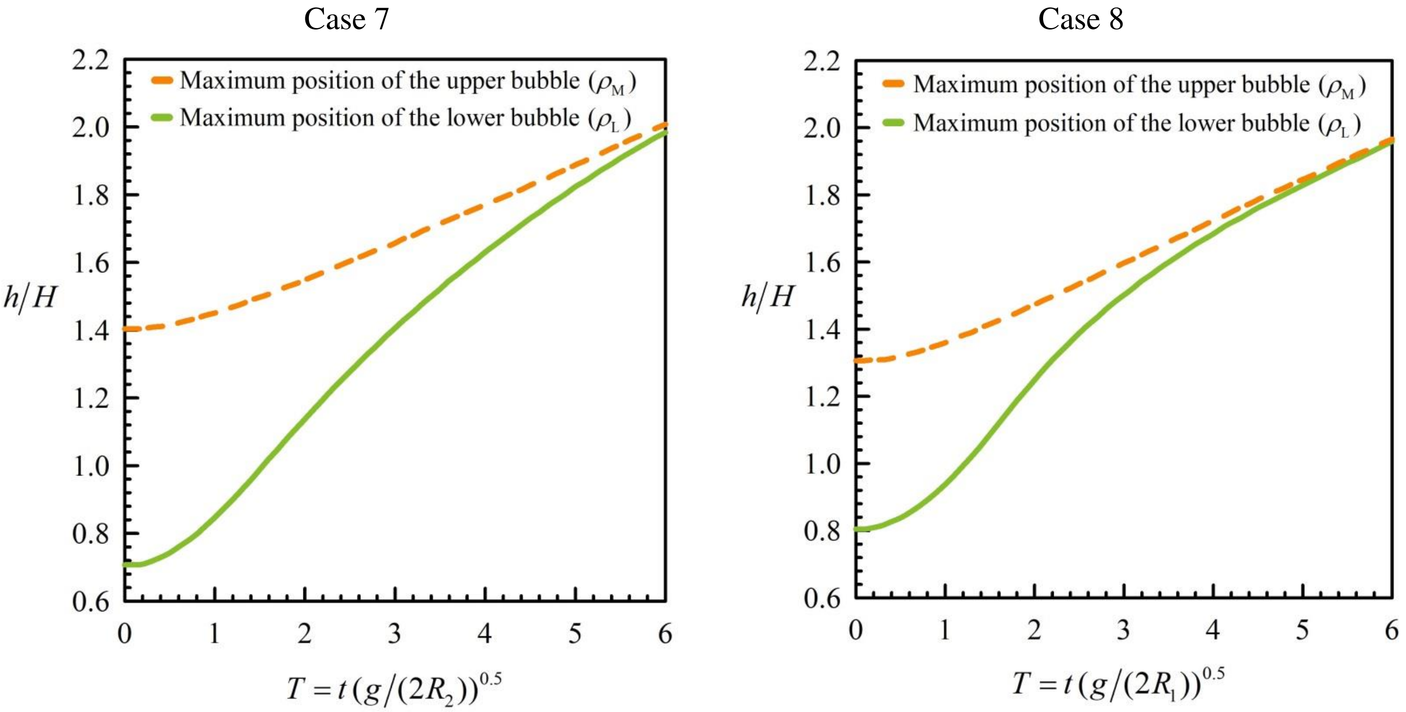

Fig. 16. The time histories of maximum locations of the bubble fronts in cases 7 and 8.

Graphical Abstract

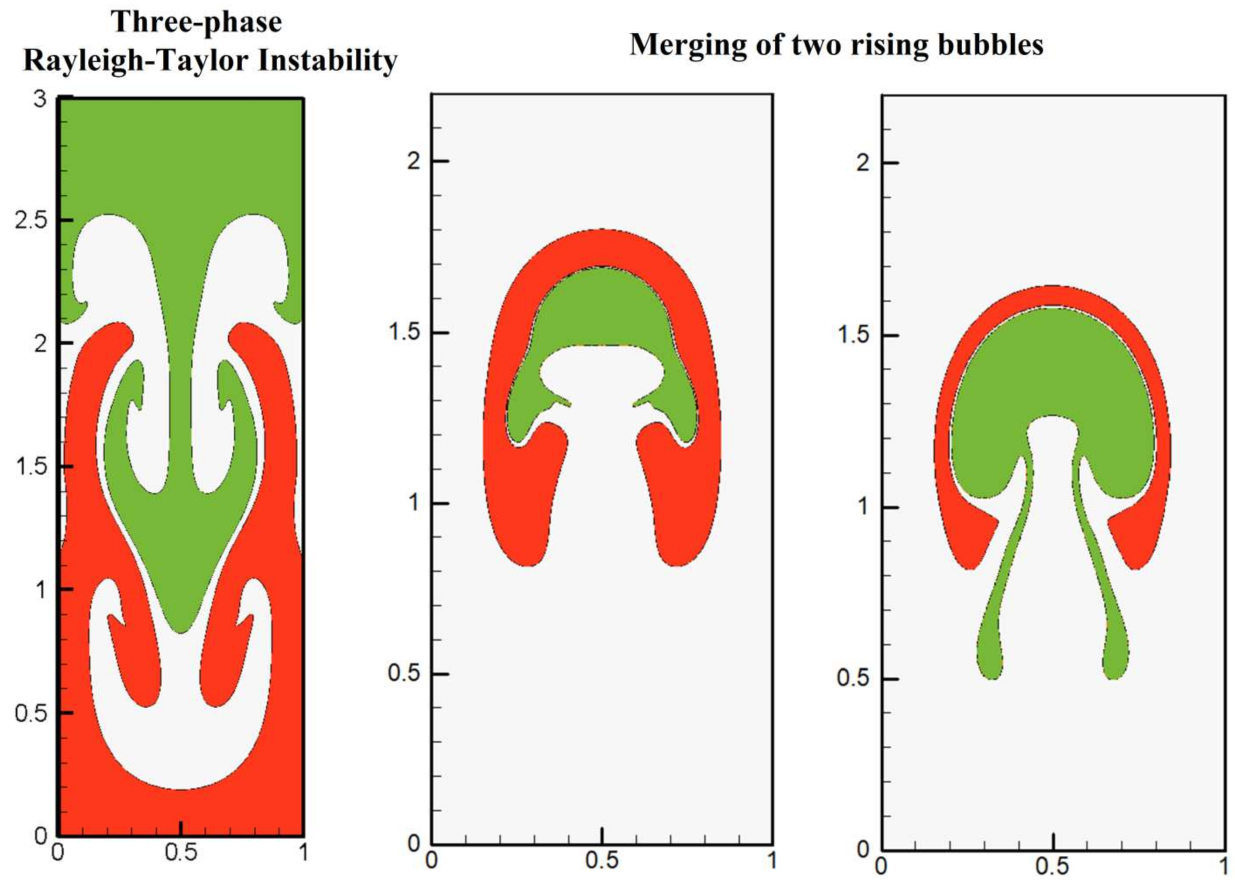

Three-phase Rayleigh-Taylor Instability

Merging of two rising bubbles